

Numerical simulation of bubble deformation and breakup under simple linear shear flows

Mitsuhiko Ohta^{a,b,*}, Tetsuya Ueta^b, Yozo Toei^c, Edwin Jimenez^d, Mark Sussman^e

^a*Department of Mechanical Science, Graduate School of Technology, Industrial and Social Sciences, Tokushima University, 2-1 Minamijyousanjima-cho, Tokushima 770-8506, Japan*

^b*Department of Mechanical Engineering, Graduate School of Technology, Industrial and Social Sciences, Tokushima University, 2-1 Minamijyousanjima-cho, Tokushima 770-8506, Japan*

^c*High Performance Plastics Company, Sekisui Chemical Co., Ltd., 2-1 Hyakuyama, Mishimagun Shimamoto-cho, Osaka 618-0021, Japan*

^d*Spectral Numerical, LLC, 1942 Broadway St., STE 314C, Boulder, CO 80302, USA*

^e*Department of Mathematics, Florida State University, Tallahassee, FL 32306, USA*

Abstract

Numerical simulations are presented for the deformation and breakup of a bubble in liquids undergoing simple linear shear flow in a variety of regimes including the low Capillary number, high Reynolds number regime. Numerical results are obtained using a projection method for incompressible two-phase flow. The method represents interfaces using the sharp interface coupled level set and Volume-Of-Fluid (CLSVOF) method. To verify the CLSVOF numerical algorithm and provide a basis for comparison, computational results are also presented that compare with previous, more popular, drop deformation and rupture simulations. The numerical results reveal that the shear-induced bubble deformation and breakup process differs significantly from that of the analogous drop system under similar flow conditions. The first distinguishing factor for bubble breakup is that the magnitude of shear flow necessary for causing rupture is much larger than that in the drop system case. In other words, a larger Reynolds number is needed to induce bubble breakup. The second distinct feature of the bubble system versus the drop system is that the bubble does not maintain a stable deformed shape as the system parameters approach the critical “breakup” Reynolds number. It is asserted that the differences in morphology for a bubble undergoing breakup versus a drop in the same process can be attributed to the density and viscosity ratio of the corresponding two-phase flow systems. The critical conditions for bubble breakup with respect to the Reynolds and capillary numbers are determined for several cases.

Keywords: Bubble deformation, bubble breakup, shear flow, CFD

*Corresponding author: m-ohta@tokushima-u.ac.jp

1 **1. Introduction**

2 Bubble dynamics in shear flow, including breakup, is critically important
3 for various gas-liquid scientific and engineering processes. We refer the reader
4 to the following experimental studies relating to bubble deformation in foaming
5 processes, microfluidic devices, microbubbles in the blood circulation system,
6 materials processing, pharmaceuticals, minerals engineering, bubble column re-
7 actor, underwater projectiles, polyethylene devolatilization, microfluidics, food
8 aeration, passive cyclonic separators, and cosmetics[7, 36, 4, 11, 12, 67, 13, 71,
9 5, 17, 70, 15, 16, 35, 52, 51, 21, 54]. In particular, it is the study of bubble de-
10 formation as it pertains to high-performance plastics applications that motivate
11 this work.

12 This article presents computational studies of shear-driven deformation and
13 breakup of a bubble in insoluble viscous liquids. Studying bubble break-up,
14 in which we focus only on the balance of the wall driving force and bubble
15 surface tension force, via computation rather than experiments simplifies the
16 process of setting a combination of precise, simple shear flow conditions, low
17 Capillary number ($Ca = \mu_m U / \sigma$) conditions, high Reynolds' number conditions
18 ($Re = \rho_m R U / \mu_m$), low-density ratio, low viscosity ratios, and zero buoyancy ef-
19 fects. We remark that previous controlled experimental studies on shear-driven
20 bubble deformation are restricted to the low Reynolds' number and large capil-
21 lary number regime[50, 5]. One reason is that buoyancy effects are minimized in
22 highly viscous liquids. On the other hand, many applications are characterized
23 by liquids in the high Reynolds' number regime. The physical properties that
24 distinguish bubble and drop studies are expressed in terms of the density ratio
25 $\lambda = \rho_b / \rho_m$ and the viscosity ratio $\eta = \mu_b / \mu_m$, where ρ is the fluid density, μ is
26 the viscosity and the subscripts "b" and "m" denote the "bubble" or "drop" and
27 the "matrix fluid", respectively. For a bubble in an insoluble, viscous liquid,
28 $\lambda \simeq 0$ and $\eta \simeq 0$, whereas most studies dealing with a drop in an immiscible
29 viscous liquid take $\lambda = 1$ and $\eta \simeq 1$.

30 In this work, we focus on identifying critical flow states numerically, in terms
31 of dimensionless quantities, that specify the extreme conditions at which a bub-
32 ble in shear flow first transitions from deformation to breakup. We validate our
33 numerical method by examining the sensitivity of the critical bubble deforma-
34 tion and break-up flow states with respect to the grid size. We also compare
35 with previous experimental results where the experimental data is available
36 (the high Capillary number low Reynolds' number regime). An advantage of
37 studying shear-driven bubble deformation and breakup computationally rather
38 than experimentally is that one can easily modify bubble/drop shape initial
39 conditions [39], the gravity force term[21], fluid physical properties, and the ge-
40 ometry of the (virtual) apparatus[16]. In our computations, the time-evolution
41 of the boundary between gas and liquid is tracked with a Coupled-Level-Set
42 and Volume-Of-Fluid (CLSVOF) sharp interface capturing algorithm [59, 61].
43 The rationale for the CLSVOF method is that the hybrid method represents
44 the (complex) gas-liquid interfaces with minimal volume loss (property of the
45 Volume-Of-Fluid method) and minimal error in the approximation of the sur-

46 face tension force (property of the Level-Set method). Our sharp interface
47 approach[61, 57, 27] enables us to simulate multiphase flows without artificially
48 giving the interface an empirical thickness.

49 We focus on determining critical physical conditions in which the breakup of
50 a bubble occurs in shear flow because it is important to identify the parameter
51 regimes in which a relatively simple system transitions from stable to unstable.
52 Specifically, we ascertain the critical Reynolds number (Re_c) corresponding to
53 the bubble breakup onset condition as a function of Ca .

54 In previous experimental or computational studies on the motion of bubble
55 deformation in a simple shear flow [5, 50, 36], only findings for bubble defor-
56 mation under very low Re number conditions ($Re \ll 1$) have been reported.
57 This is understandable since a low Reynolds number matrix fluid mitigates the
58 effect of gravity on distorting the comparison with the drop case. In the results
59 reported in [5], the $x - z$ cross section of the deforming bubble was close to
60 circular in their experiments. Also in the experiments in [5], the $x - z$ cross
61 section shows minimal overall bubble rise speed in the (very) viscous fluid in
62 comparison to the rate that the bubble deforms in the $y - z$ cross section. This
63 is expected since the experiments designed by [5] closely followed the following
64 basic assumptions: (i) “steady creeping flow with negligible inertial effects,” (ii)
65 “Incompressible Newtonian fluids,” (iii) “No buoyancy effects,” (iv) “No wall
66 effects.” In this work, we determine, for the first time, the critical Reynolds
67 number ($Re \gg 1$) that leads to bubble breakup. Additionally, our computa-
68 tional studies reveal characteristics that distinguish a drop’s deformation and
69 breakup processes versus those of a bubble.

70 We remark that there have been a number of computational articles on the
71 study of lift of slightly deformable bubbles[14, 31]. We reiterate, though, that
72 for bubble deformation and breakup in shear flows, only a few computational
73 articles exist: [69, 68, 53]. These previous studies mainly examined the dynamics
74 (e.g., rotation angle) of bubble deformation in shear flow. Concerning bubble
75 breakup, Wei et al. [69] presented one numerical result for a bubble breakup
76 process under the condition of Ca (capillary number) = 35. Sharifi et al[53]
77 presented two results for bubble breakup corresponding to $Ca = 7.5$ and $Ca =$
78 11.2. We point out that all of the previous computational research on bubble
79 deformation (and breakup) under shear driven flow[69, 68, 53] use the (explicit)
80 Lattice Boltzmann method. For accurately computing the tensile strength of a
81 bubble, and accurately computing threshold parameters for break-up (what we
82 do in this article, and what was not done in previous work), it is critical that a
83 numerical method directly enforces the velocity continuity condition and the gas-
84 liquid interface normal jump conditions. We contend that a projection method
85 (i.e. this paper and [73, 74, 41]) is the more appropriate (albeit slower) method
86 for our study rather than the Lattice Boltzmann method. Also, in contrast to
87 the Lattice Boltzmann method, our interface “capturing” method, the CLSVOF
88 method[59, 61], maintains the gas/liquid interface as sharp, enables accurate
89 approximation of the surface tension force, and by construction the CLSVOF
90 method preserves mass and volume within a fraction of a percent. The results
91 that we present in this article (see e.g. section 3.3.2) regarding measuring the

tensile strength of a bubble are unique and validated with respect to comparisons with previous experimental data (where available) and grid refinement studies. Admittably, each simulation on the finest resolution takes over a half a year to complete on a workstation because of the following unavoidable factors: (i) the large density-ratio projection method requires the solution of a large sparse, ill-conditioned, matrix system at each time step, (ii) the finer the mesh, the more precise the measured threshold, and right at the threshold (Taylor Deformation parameter $D \approx 1!$), oscillatory behaviour is observed delaying the determination of breakup or not. Finally, the larger the deformation parameter D , the longer one must make the computational domain (and thereby leading to larger domain aspect ratio) thereby adversely effecting the condition number even more for carrying our the pressure projection.

To highlight the mechanisms of bubble deformation and breakup in a shear flow, we juxtapose the bubble results with those of a drop. We remark that while the study of critical tensile strength parameters for the bubble is sparse, there have been many studies for the simpler drop problem. This is because the density ratio for the drop deformation case is almost one so that it is not required that the continuous phase liquid be highly viscous in order to mitigate buoyancy effects. For completeness, we give a brief overview of previous “tensile strength” studies pertaining to drops.

The study of the deformation and breakup of a drop in immiscible viscous liquids undergoing simple linear shear flow has been investigated extensively due to its fundamental importance to emulsion processes, materials processing, mixing, and reaction devices. The pioneering experimental work on this problem was performed by Taylor in the early 1930s [64, 65], and the subsequent theoretical and experimental progress up to the 1980s and 1990s was reviewed in [43] and [56], respectively. By the 2000s, progress in computational fluid dynamics (CFD) techniques and increased access to powerful computing resources led to a surge of research focused on direct simulations of this problem. In particular, detailed computational investigations of drop breakup, based on a Volume-of-Fluid (VOF) method [20] were presented in [33, 47, 49, 48, 28, 44, 45, 46]. Since then, the literature on computational studies on the deformation and breakup of a single or several drops in shear flow has continued to grow [9, 23, 72, 3, 25, 10, 29, 30, 24, 19, 1, 75] and a variety of numerical techniques have been developed to tackle this problem, including boundary-integral approaches [8, 26], lattice Boltzmann methods [22, 29], front tracking schemes [66], and interface-capturing level set methods [60].

Thus, a lot of studies about the deformation and breakup of a drop in simple linear shear have been presented so far. In contrast, few studies have been conducted on bubble deformation and breakup. In the low Capillary number, high Reynolds’ number regime, there are no controlled experiments or simulations. We reiterate why there have been few studies regarding the “tensile strength” of bubbles. Experimentally, if one wants to isolate the interplay of shearing force with the bubble surface tension force, in the moderate to high Reynolds number regime, and low Capillary number regime, one is restricted to microgravity conditions. Computational experiments are difficult too. In

138 order to accurately compute the tensile strength of a bubble, one must resort
 139 to a combination of parallel computing, the multigrid preconditioned conjugate
 140 gradient method[63, 61] for poorly conditioned large sparse matrix systems,
 141 adaptive mesh refinement[76, 61], and a robust, volume preserving interface
 142 tracking method (we use the CLSVOF method[59, 61]). These aspects of our
 143 algorithm allow one to accurately simulate the balance of the restoring bubble
 144 surface tension force against the driving wall shear force and at the same time,
 145 accurately simulate the evolution of the bubble shape to bubble-break-up if the
 146 given shear stress and physical properties permit it.

147 2. Problem Description

148 Figure 1(a) shows a schematic of the computational system for our studies
 149 of a bubble (or drop) in shear flow. The computational domain consists of a
 150 three-dimensional rectangular domain with the dimensions of L (length) $\times W$
 151 (width) $\times H$ (height). The size of L , W and H was determined after considera-
 152 tion of the sensitivity of numerical results to the domain size; numerical studies
 153 of domain-size dependence are presented in Section 3.3. All computational re-
 154 sults that follow were obtained from numerical solutions of the three-dimensional
 155 governing equations for gas-liquid/liquid-liquid flows. Computations are initial-
 156 ized with a spherical bubble (or drop) of radius $R = 5$ mm set at the center of
 157 the computational domain. The bubble (or drop) is then subjected to a linear
 158 shear flow generated by the motion of the top and bottom plates, which have
 159 constant velocity $+V$ and $-V$, respectively. In the interior of the domain, the
 160 initial velocity condition is assumed to be a simple linear profile and periodic
 161 boundary conditions are imposed along the x and y directions. Mathematically,
 162 the initial and boundary conditions are described as follows:

$$\phi(x, y, z, 0) = \sqrt{(x - \frac{L}{2})^2 + (y - \frac{W}{2})^2 + (z - \frac{H}{2})^2} - R \quad (1)$$

$$\mathbf{u}(x, y, z, 0) = \begin{pmatrix} \frac{2V}{H}(z - \frac{H}{2}) \\ 0 \\ 0 \end{pmatrix}$$

$$\phi(x + L, y, z, t) = \phi(x, y, z, t) \quad \phi(x, y + W, z, t) = \phi(x, y, z, t)$$

$$\mathbf{u}(x, y, H, t) = \begin{pmatrix} V \\ 0 \\ 0 \end{pmatrix} \quad \mathbf{u}(x, y, 0, t) = \begin{pmatrix} -V \\ 0 \\ 0 \end{pmatrix}$$

$$\mathbf{u}(x + L, y, z, t) = \mathbf{u}(x, y, z, t) \quad \mathbf{u}(x, y + W, z, t) = \mathbf{u}(x, y, z, t)$$

163 $\phi(x, y, z, t)$ is a material indicator function which is positive in the “matrix”
 164 fluid and negative in the bubble (or drop) fluid. $\mathbf{u}(x, y, z, t)$ is the velocity.

165 Common dimensionless physical parameters used to describe gas-liquid or
 166 liquid-liquid two-phase flows include the Reynolds (Re), Weber (We) (or Ca (=
 167 We/Re)) and Froude (Fr) numbers. Gas-Liquid and Liquid-Liquid two-phase
 168 flow problems are also determined by the density ratio λ and the viscosity ratio

¹⁶⁹ η . In the present study, in order to clearly isolate the effects of λ and η , and
¹⁷⁰ isolate the balance of the driving wall force with the bubble surface tension
¹⁷¹ force, the effect of gravity is not considered ($g = 0$) so that we ignore the effect
¹⁷² of the Fr number ($= \frac{\Gamma R}{\sqrt{gR}}$).

¹⁷³ When comparing with previous drop studies, we fix $\lambda = 1$ for the drop cases.
¹⁷⁴ As a result, (for $\lambda = 1$) the following dimensionless physical parameters are used
¹⁷⁵ to describe the problem of drop deformation/breakup in shear flow:

$$Re = \frac{\rho_m U R}{\mu_m}, \quad Ca = \frac{\mu_m U}{\sigma}, \quad \eta = \frac{\mu_b}{\mu_m} \quad m = \text{matrix fluid} \quad (2)$$

¹⁷⁶ U is the velocity scale and σ denotes the surface tension. For the problem of
¹⁷⁷ shear-induced drop deformation and breakup, the velocity is set to,

$$U = \Gamma R,$$

¹⁷⁸ where the shear-rate is,

$$\Gamma = 2V/H.$$

¹⁷⁹ As mentioned in the introduction, most previous drop studies set $\eta = 1$ (e.g. Li
¹⁸⁰ et al. [33]). Thus, for comparison with previous drop deformation and breakup
¹⁸¹ problems, we set $\lambda = \eta = 1$ (and also neglect the effect of gravity so that
¹⁸² $g = 0$). On the other hand, in our computations for bubble deformation, we
¹⁸³ set the density and viscosity of air to be $\rho_b = 1.2 \text{ kg/m}^3$ and $\mu_b = 1.8 \times 10^{-5}$
¹⁸⁴ Pa·s respectively. We emphasize that for consistency with previous studies (Li
¹⁸⁵ et al. [33], Rust and Manga [50], Müller-Fischer et al. [36], Komrakova et al.
¹⁸⁶ [29], Amani et al. [1]), we computationally examine the deformation and breakup
¹⁸⁷ of a bubble in simple linear shear flow as a function of the Re and Ca numbers.
¹⁸⁸ That is to say, by setting $g = 0$, we are isolating the effect of only varying Re and
¹⁸⁹ Ca on bubble deformation and breakup. In our controlled study, we determine
¹⁹⁰ the critical Re_c versus Ca curve in which Re_c corresponds to the threshold of
¹⁹¹ bubble (or drop) breakup. We determine the critical Re_c versus Ca curve for
¹⁹² strategic pairs of the density ratio and viscosity ratio.

¹⁹³ In our computations, the density of the matrix fluid is fixed at $\rho_m = 1000$
¹⁹⁴ kg/m^3 . The surface tension at the bubble (drop) interface is $\sigma = 2.5 \times 10^{-2}$
¹⁹⁵ N/m. The values of Re and Ca in our simulations are controlled by changing
¹⁹⁶ the values of μ_m and V . Specifically, we set $\mu_m = 2.0 \times 10^{-2} \sim 6.0 \times 10^{-2}$
¹⁹⁷ Pa·s and $V = \text{about } 1.1 \sim 1.3 \text{ m/s}$. As a consequence, for studying bubble
¹⁹⁸ deformation and break-up, the density and viscosity ratios satisfy $\lambda = 1.2 \times 10^{-3}$
¹⁹⁹ and $\eta < 1.0 \times 10^{-3}$.

²⁰⁰ Remark: if we were to apply “Earth” gravity conditions in our simulations,
²⁰¹ then $g = 9.8 \text{ m/s}^2$, and the Froude number (Fr) is in the range $Fr = 1.7 \sim 1.9$.
²⁰² Although these values of Fr are not so large, the effect of gravity (inducing
²⁰³ bubble rise motion) may not be completely negligible. However, bubbles in
²⁰⁴ our computations reach the breakup by way of deformation very quickly at t
²⁰⁵ = about 0.5 s. Accordingly, it is expected that the effect of gravity (inducing
²⁰⁶ bubble rise motion) can be small for the behavior of bubble deformation and
²⁰⁷ breakup around the critical Re number conditions determined in our study.

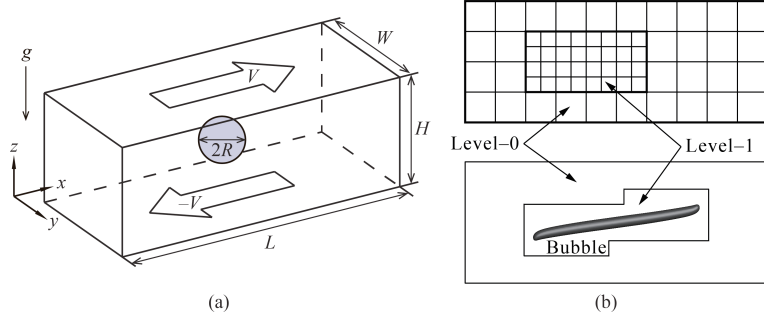


Figure 1: (a) Computational domain schematic for a bubble or drop in shear flow. Gravity is set to zero in our computations in order to isolate the effects of density and viscosity ratios. (b) (upper panel) a two-level adaptive mesh refinement (AMR) grid schematic corresponding to one of our simulations; (lower panel) snapshot of bubble deformation in simple linear shear flow.

208 3. Numerical Analysis

209 3.1. Numerical method and governing equations

210 Numerical results were obtained using the interface capturing Coupled Level
 211 Set and Volume of Fluid (CLSVOF) method (Sussman and Puckett [59], Suss-
 212 man et al. [61]), which is based on a fixed grid finite volume algorithm. The
 213 CLSVOF method is a robust numerical technique that combines some of the ad-
 214 vantages of the Volume of Fluid (VOF) method (Hirt and Nichols [20]) and the
 215 Level Set (LS) (Sussman et al. [60]) method while overcoming their weaknesses.
 216 In the VOF method, the Volume Fraction function, F , is used to represent
 217 the interface. The values of F correspond to the volume fraction of liquid in
 218 a given computational cell. In other words, $F = 0$ when a computational cell
 219 contains only gas and $F = 1$ when a computational cell contains only liquid.
 220 If $0 < F < 1$, then a computational cell contains the gas-liquid interface. The
 221 VOF method has an advantage over the LS method in that accurate algorithms
 222 for advecting F can be applied so that mass/volume is conserved up to machine
 223 precision while still maintaining a sharp representation of the interface. On
 224 the other hand, the disadvantage of the VOF method in comparison to the LS
 225 method is that tangled and difficult reconstruction procedures are required for
 226 determining the slope of the piecewise linear VOF reconstructed interface. In
 227 the LS method, the signed distance function ϕ (LS function) is used to track the
 228 interface. The interface is implicitly represented by the set of points in which
 229 $\phi = 0$. Liquid and gas regions are defined as $\phi > 0$ in the liquid and $\phi < 0$ in the
 230 gas, respectively. One of the advantages of the LS method is that one can track
 231 and represent smoothly the interface, but the LS method has the disadvantage
 232 that mass/volume is not explicitly conserved. In the CLSVOF method, the cou-
 233 pling between the LS function and the VOF function occurs when computing
 234 the normal of the reconstructed interface in the VOF calculation process and
 235 also when assigning the LS function with the exact signed normal distance to
 236 the reconstructed interface in the LS calculation process. That is to say, the

piecewise linear approximation (the volume-of-fluid reconstruction step) for the VOF method is determined using the unit normal vector (\mathbf{n}) estimated from information of the LS function. By taking advantage of both methods, the evolution of the liquid-gas interface location can be computationally captured in such a way so that volume/mass is preserved to machine precision and at the same time, the interface normals and the surface tension force (which is proportional to the interface curvature) can be straightforwardly derived from the smooth level set function.

In our studies, the two-phase fluid flow is comprised of air and a viscous Newtonian liquid. The Heaviside function, $\mathcal{H}(\phi)$, which is defined as

$$\mathcal{H}(\phi) = \begin{cases} 1 & \phi \geq 0 \\ 0 & \phi < 0 \end{cases} \quad (3)$$

will be used below to distinguish each of the two fluids. A single set of three-dimensional equations governs the motion of both fluids, which are taken to be incompressible, and consists of the continuity equation and the Navier-Stokes equations with surface tension forces:

$$\nabla \cdot \mathbf{u} = 0 \quad (4)$$

$$\frac{\partial \mathbf{u}}{\partial t} + (\mathbf{u} \cdot \nabla) \mathbf{u} = \frac{1}{\rho} \nabla \cdot (-p \mathbf{I} + 2\mu \mathbf{D}) + \mathbf{g} - \frac{\sigma\kappa}{\rho} \nabla \mathcal{H} \quad (5)$$

We remark that our method is a “sharp interface method[61, 57, 27]. Thereby we do not need to specify an empirical interface thickness parameter[60, 59].

\mathbf{u} is the velocity vector, t represents time, p is the pressure, \mathbf{I} is the unit tensor, \mathbf{D} is the rate of deformation tensor ($\mathbf{D} = \frac{1}{2}(\nabla \mathbf{u} + (\nabla \mathbf{u})^T)$), ρ is the density, μ is the viscosity, κ is the interfacial curvature, and the Heaviside function $\mathcal{H}(\phi)$ is a function of the level set (LS) function ϕ . The singular Heaviside gradient term in the right-hand side of equation (5) is a body force representing the surface tension force and is equivalent to specifying that the jump in the normal stress is equal to $\sigma\kappa$ (Tanguy et al. [62]). The surface tension force expressed by the singular Heaviside gradient term acts only on the gas-liquid interface. The sharp interface “Ghost Fluid Method” (Kang et al. [27]) is used to discretize the gradient of the Heaviside function as it appears in the surface tension force term. This force, upon discretization, is only non-zero across cells in which the level set function changes sign.

The interfacial curvature κ is computed with second-order accuracy directly from the volume-of-fluid (VOF) function and the level set function using the height function technique (Sussman [57], Sussman et al. [61]). We remark that we would get the same results if we compute κ directly from the LS function using the “level set” height function technique.

Since ρ and μ are taken to be constant in each fluid, with a jump at the interface, they can be expressed in terms of the Heaviside function,

$$\rho = \rho_m \mathcal{H} + \rho_b (1 - \mathcal{H}), \quad \mu = \mu_m \mathcal{H} + \mu_b (1 - \mathcal{H}). \quad (6)$$

²⁷² The subscripts “b” and “m” refer to “bubble” (or drop) and “matrix fluid.”
²⁷³ To represent the free surface with the CLSVOF method, we must evolve the
²⁷⁴ solution to both the VOF equation for F and the LS equation for ϕ :

$$\frac{\partial F}{\partial t} + (\mathbf{u} \cdot \nabla) F = 0, \quad \frac{\partial \phi}{\partial t} + (\mathbf{u} \cdot \nabla) \phi = 0. \quad (7)$$

²⁷⁵ In all computations, the discretized variables p , ϕ , and F are located at the
²⁷⁶ cell centers, and the discrete velocity variable \mathbf{u} is located at the cell face cen-
²⁷⁷ ters. Our computations are performed using an overall second-order accurate
²⁷⁸ hydrodynamic scheme. The spatial discretization uses second-order accurate,
²⁷⁹ slope-limited, upwind techniques for the nonlinear advective terms. The ve-
²⁸⁰ locity and pressure fields are computed using an implicit pressure projection
²⁸¹ procedure.

²⁸² The temporal discretization of our numerical method is an operator split
²⁸³ projection method as described by Sussman et al. [61]. An outline of our method
²⁸⁴ is as follows (see Sussman et al. [61], section 4, for more details):

All Steps. Timestep

²⁸⁵ The timestep, Δt , is governed by the CFL condition and surface tension
²⁸⁶ (section 5.7 of Sussman et al. [61]):

$$\Delta t < \min_{i,j,k} \left(\frac{\Delta x}{2|U^n|}, \frac{1}{2} \sqrt{\frac{\rho^L}{8\pi\sigma}} \Delta x^{3/2} \right)$$

Step 1. CLSVOF interface advection

$$\begin{aligned} \phi^{n+1} &= \phi^n - \Delta t [\mathbf{u} \cdot \nabla \phi]^n \\ F^{n+1} &= F^n - \Delta t [\mathbf{u} \cdot \nabla F]^n \end{aligned}$$

Step 2. Nonlinear advective force terms

$$\mathcal{A} = [\mathbf{u} \cdot \nabla \mathbf{u}]^n$$

Step 3. Viscosity force

$$\frac{\mathbf{u}^* - \mathbf{u}^n}{\Delta t} = -\mathcal{A} + g\vec{z} - [\nabla p / \rho]^n + \frac{1}{2} \frac{\nabla \cdot (2\mu \mathbf{D}^n) + \nabla \cdot (2\mu \mathbf{D}^*)}{\rho}$$

²⁸⁷ Step 4. Pressure projection and ghost fluid surface tension algorithm

$$\mathbf{V} = \mathbf{u}^n + \Delta t (-\mathcal{A} + g\vec{z} + \frac{1}{2} \frac{\nabla \cdot (2\mu \mathbf{D}^n) + \nabla \cdot (2\mu \mathbf{D}^*)}{\rho})$$

288

$$\mathbf{V} = \mathbf{V} - \Delta t \frac{\sigma \kappa(\phi^{n+1})}{\rho} \nabla \mathcal{H}(\phi^{n+1})$$

289

$$\nabla \cdot \frac{\nabla p}{\rho} = \frac{1}{\Delta t} \nabla \cdot \mathbf{V}$$

290

$$\mathbf{u}^{n+1} = \mathbf{V} - \Delta t \frac{\nabla p}{\rho}$$

291 To make efficient use of computational resources, our numerical simulations
 292 utilize an adaptive hierarchy of grids based on a dynamic adaptive mesh refine-
 293 ment (AMR) technique (Sussman et al. [58]). Adaptive grids are dynamically
 294 adjusted based on the location of the deforming gas-liquid interface. In the
 295 AMR technique, the grid resolution is increased in regions near the interface,
 296 while a coarser grid is used where the flow is relatively steady. The upper panel
 297 of Figure 1(b) displays a schematic view of the hierarchical grid structure, and
 298 the lower panel corresponds to an actual computational example corresponding
 299 to bubble deformation in simple linear shear flow. In general, the mesh hier-
 300 archy is composed of different levels of refinement ranging from coarsest $\ell = 0$
 301 (“level-0”) to finest $\ell = \ell_{\max}$ (“level- ℓ_{\max} ”). The refinement ratio of one grid
 302 size ($\Delta x = \Delta y = \Delta z$) to the next finer level is two so that $\Delta x^{\ell+1} = 0.5 \Delta x^\ell$. All
 303 computations in this study used an AMR system with a maximum prescribed
 304 level $\ell_{\max} = 1$ (as illustrated in the upper panel of Figure 1(b)). In our adaptive
 305 mesh refinement algorithm, the velocity in the coarse grid cells that neighbor
 306 fine grid cells are interpolated from the coarse grid using bilinear interpolation to
 307 initialize “ghost” fine cells. Thus, the bilinear interpolation procedure produces
 308 interpolated fine-grid data as a linear combination of the coarse-grid data.

309 Remark 1: Due to time step stability constraints, the variable density pres-
 310 sure projection process, and computed bubble shapes with high aspect ratio,
 311 we find that our simulations can take over six months. We have experimented
 312 with (a) decreasing the “error buffer” parameter from two cells to one (radius
 313 of cells to be tagged when a given cell is tagged for adaptivity) and (b) relaxing
 314 the condition that the bubble-liquid interface be wholly contained on the finest
 315 adaptive level. Unfortunately, we have found that these steps lead to poorer
 316 accuracy. This “diminishing returns” phenomenon is expected for low Mach
 317 number flows in which the incompressible flow equations are characterized by
 318 non-local behavior. We refer the reader to the following research[34] in which
 319 it has been found through a systematic study that using an AMR grid can be
 320 less accurate than a case with a uniform fine grid (luckily, that is not the case
 321 here). To summarize, we have found that each further refinement of the grid
 322 will multiply the simulation time by about eight (a factor of 4 due to spatial
 323 refinement and a factor of 2 due to temporal refinement).

324 Remark 2: We believe that including a customized sub-scale model right
 325 at the point of bubble break-up is unnecessary because the driving shear force

326 is uniformly applied in the time variable instead of impulsively applied. We
 327 are aware of research for predicting whether droplets merge or bounce[32] that
 328 necessitate the inclusion of a sub-scale model, but that research is not applicable
 329 in our case. Previous studies on the shear flow-driven breakup of bubbles or
 330 drops have not incorporated customized subscale models[33, 29, 1].

331 *3.2. Validation of the numerical method*

332 The effectiveness of our sharp interface computational method has been
 333 demonstrated via grid refinement studies and comparison with experiments for
 334 the complicated rising motion of single bubbles and drops in viscous liquids
 335 Ohta and Sussman [41], Ohta et al. [37, 38, 42], Stewart et al. [55], Sussman
 336 et al. [61], the simulation of atomization in a realistic diesel injector[2], and the
 337 simulation of bubble formation due to the injection of gas through a nozzle[40].
 338 In this section, the accuracy of our computational method will be verified for
 339 the problem of shear-induced deformation of a drop and bubble.

340 First, we compare quantitatively against the steady-state drop deformation
 341 results reported by Li et al. [33]. The shape of a deformed drop in simple
 342 linear shear flow is described in terms of the Taylor deformation parameter
 343 $D=(a-b)/(a+b)$, where a and b are the major and minor axes of the deformed
 344 drop, respectively. For consistency, we perform numerical simulations using
 345 CLSVOF over the same computational domain and grid size used in Li et al. [33],
 346 which has dimensions $L(8R) \times W(4R) \times H(8R)$ (recall that R is the bubble/drop
 347 radius) and a level-0 grid size $\Delta x = \Delta y = \Delta z = R/8$; our two-level AMR grid
 348 structure also uses a finer level-1 grid size $\Delta x^{\ell=1} = \Delta y^{\ell=1} = \Delta z^{\ell=1} = R/16$.
 349 Numerical results are listed in Table 1 for D as a function of Re , with $Ca = 0.3$
 350 and $\lambda = \eta = 1$ fixed in every case. The results in Table 1 compare computations
 351 using our CLSVOF algorithm with corresponding results obtained with the VOF
 352 method used in Li et al. [33].

Table 1: Comparison of the Taylor deformation parameter D for a drop as a function of Re ($Ca = 0.3$, $\lambda = \eta = 1$). In all cases, the domain size is $L(8R) \times W(4R) \times H(8R)$, where R is the drop radius. The CLSVOF method computations used a two-level AMR computational domain with a level-0 discretization $\Delta x^{\ell=0} = \Delta y^{\ell=0} = \Delta z^{\ell=0} = R/8$ and a level-1 discretization $\Delta x^{\ell=1} = \Delta y^{\ell=1} = \Delta z^{\ell=1} = R/16$.

Reynolds number	0.1	0.5	0.6	0.75
D (Li et al. [33])	0.3968	0.45	0.4768	Breakup
D (Our study)	0.3960	0.4570	0.4758	Breakup

352 Next, we report the results of validation tests conducted with our computa-
 353 tional method; we compare our results with the “bubble deformation in simple
 354 linear shear flow” results reported by Müller-Fischer et al. [36]. Müller-Fischer
 355 et al. [36] experimentally inquired into the bubble deformation under the condi-
 356 tion of $Re \approx 0$. In our study, we computed the bubble deformation on a compu-
 357 tational domain with dimensions $L(12R) \times W(6R) \times H(6R)$ and a computational
 358 grid in which the finest level grid size was $\Delta x^{\ell=1} = \Delta y^{\ell=1} = \Delta z^{\ell=1} = R/16$.
 359

360 Computations were performed for the conditions of $Ca = 0.96$ and $Ca = 1.63$
 361 with $Re \approx 0$ ($Re = 5.0 \times 10^{-4}$), $\lambda = 1.2 \times 10^{-3}$ and $\eta \leq 1.2 \times 10^{-6}$. The pre-
 362 scribed parameters are consistent with the experimental conditions by Müller-
 363 Fischer et al. [36]. Comparisons of our numerical results and previous experi-
 364 mental results (Müller-Fischer et al. [36]) are tabulated in Table 2. Addition-
 365 ally, in Table 2, we list experimental results with the condition of $Re \approx 0$ and
 366 $\lambda \approx \eta \approx 0$ by Rust and Manga [50]. These experimental values were obtained
 367 from the graph showing the relation of D vs Re (Rust and Manga [50]). As is
 368 clear from Table 2, our numerical results predicted larger values of D than experi-
 369 mental ones reported by Müller-Fischer et al. [36]. Nevertheless, our numerical
 370 results are very close to the experimental results by Rust and Manga [50], which
 371 emphasizes the intrinsic difficulties associated with experimental investigations
 372 of bubble dynamics, even in simple linear shear flow. These comparisons suggest
 373 that our computational method is effective and robust at reproducing bubble
 dynamics in simple linear shear flow.

Table 2: Comparison of D for a bubble as a function of Ca ($Re \approx 0$, $\lambda \approx \eta \approx 0$). In all cases, the domain size is $L(12R) \times W(6R) \times H(6R)$. The CLSVOF computations used a two-level AMR computational domain with a level-0 discretization $\Delta x^{\ell=0} = \Delta y^{\ell=0} = \Delta z^{\ell=0} = R/8$ and a level-1 discretization $\Delta x^{\ell=1} = \Delta y^{\ell=1} = \Delta z^{\ell=1} = R/16$.

Capillary number	0.96	1.63
D (Müller-Fischer et al. [36])	0.37	0.58
D (Rust and Manga [50])	0.71 ± 0.05	0.81 ± 0.02
D (Our study $\Delta x^{\ell=1} = R/16$)	0.63	0.71

374 Finally, we compare numerical results from our method with the numerical
 375 results for drop breakup reported in Renardy and Cristini [49]. Figure 2 demon-
 376 strates drop breakup with pinch-off behavior for three Re and Ca conditions
 377 and with constant values of $\lambda = \eta = 1$ for all cases. The three cases that we
 378 consider correspond to (a) $Re = 10$, $Ca = 0.16$, (b) $Re = 12$, $Ca = 0.1753$,
 379 and (c) $Re = 15$, $Ca = 0.196$, and which are illustrated in Figures 2(a)-(c),
 380 respectively. The results reported in Renardy and Cristini [49], which were
 381 obtained with a VOF method, are shown inside boxes while results obtained
 382 with our CLSVOF approach are displayed outside boxes. In the computations
 383 presented in Renardy and Cristini [49], the dimensions $W = 4R$ and $H = 8R$
 384 were fixed, while L was changed depending on Re and Ca conditions, and
 385 the grid size was set to $\Delta x = \Delta y = \Delta z = R/8$. To compare with their re-
 386 sults, we performed simulations with the CLSVOF method over a two-level
 387 AMR computational domain of the same dimensions and the same level-0 dis-
 388 cretization: $\Delta x^{\ell=0} = \Delta y^{\ell=0} = \Delta z^{\ell=0} = R/8$; we set the finer level-1 grid size
 389 $\Delta x^{\ell=1} = \Delta y^{\ell=1} = \Delta z^{\ell=1} = R/16$. The results shown in Figure 2 verify that our
 390 numerical approach can reproduce the same drop breakup behavior presented
 391 in Renardy and Cristini [49]. Slight differences between the results can be at-
 392 tributed to the increased resolution used in our study in the level-1 grid around
 393 the elongated drop.

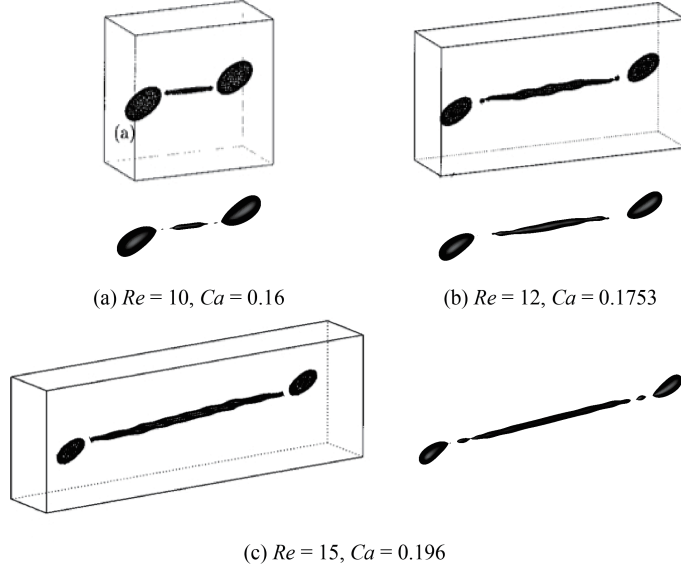


Figure 2: Comparison with results reported in Renardy and Cristini [49] (shown in bounding boxes) for drop breakup in shear flow. In Renardy and Cristini [49], the computational domain dimensions were $W = 4R$, $H = 8R$, and L was varied depending on the Re and Ca conditions. The grid size in Renardy and Cristini [49] was set to $\Delta x = \Delta y = \Delta z = R/8$. Reprinted with permission from reference Renardy and Cristini [49]. Copyright 2001, AIP Publishing. The results obtained with our CLSVOF algorithm, corresponding to each case in reference Renardy and Cristini [49], are shown without the bounding boxes. The CLSVOF method used a two-level AMR computational domain with a level-0 discretization $\Delta x^{\ell=0} = \Delta y^{\ell=0} = \Delta z^{\ell=0} = R/8$ and a level-1 discretization $\Delta x^{\ell=1} = \Delta y^{\ell=1} = \Delta z^{\ell=1} = R/16$. The onset of drop breakup is demonstrated for (a) $Re = 10, Ca = 0.16$, (b) $Re = 12, Ca = 0.1753$, and (c) $Re = 15, Ca = 0.196$. For all three Re and Ca conditions, $\lambda = \eta = 1$.

395 The numerical validation studies performed in this section and the follow-
 396 ing section demonstrate that our numerical method can reliably determine the
 397 transition regions at which shear-induced bubble or drop deformation leads to
 398 breakup. In the next section, we demonstrate that we can expect an error of 3%
 399 for predicting the transition to break-up. The analysis in this section and the
 400 following also indicate that the error is reduced by a factor of 2 each time the
 401 grid is refined by a factor of 2. We reiterate that we have found at least a factor
 402 of 2 error reduction for each grid refinement in many multiphase flow problems
 403 involving complex interface deformation and breakup; see Ohta and Sussman
 404 [41], Ohta et al. [37, 38, 42], Stewart et al. [55], Sussman et al. [61], Arienti et al.
 405 [2], Ohta et al. [40].

406 3.3. Consideration of domain and grid sizes

407 3.3.1. Selecting the appropriate domain size

408 The computational domain size used in numerical studies can affect the
 409 behavior of drop deformation and breakup. Referring to Figure 1(a), with an

appropriately large domain length L and a fixed width $W = 4R$, the effect of the height H on drop behavior was examined in Li et al. [33] for Stokes flows and various Ca conditions and in Komrakova et al. [29] for $Re = 1$ and $Ca = 0.27$. Other related studies investigated drop breakup sensitivity (Renardy and Cristini [47]) and drop deformation sensitivity (Renardy et al. [48]) with respect to the entire domain size. Here, we investigate the drop dynamics sensitivity

Table 3: Comparison of the Taylor deformation parameter D for a drop as a function of domain size ($Re = 0.75$, $Ca = 0.3$, $\lambda = \eta = 1$). CLSVOF method computations used a two-level AMR computational domain with a level-0 discretization $\Delta x^{\ell=0} = \Delta y^{\ell=0} = \Delta z^{\ell=0} = R/8$ and a level-1 discretization $\Delta x^{\ell=1} = \Delta y^{\ell=1} = \Delta z^{\ell=1} = R/16$.

System	Domain size ($L \times W \times H$)	D
System 1	$8R \times 4R \times 8R$	Breakup
System 2	$12R \times 4R \times 8R$	Breakup
System 3	$8R \times 4R \times 6R$	0.541
System 4	$8R \times 6R \times 6R$	0.466
System 5	$8R \times 8R \times 8R$	0.460
System 6	$8R \times 16R \times 16R$	0.460

to domain size around the critical Reynolds number $Re_c = 0.75$. Specifically, we consider domain size sensitivity for the condition of $Re = 0.75$, $Ca = 0.3$, and $\lambda = \eta = 1$, a condition used in the comparison studies of the previous section. As shown in Table 1, the drop breaks up for the condition of $Re = 0.75$ and $Ca = 0.3$ with a domain size of $L(8R) \times W(4R) \times H(8R)$. Results for domain size sensitivity for six domain systems, all of which use a level-1 grid size $\Delta x^{\ell=1} = \Delta y^{\ell=1} = \Delta z^{\ell=1} = R/16$, are tabulated in Table 3. Note that the domain size used in the comparison study (Table 1) corresponds to System 1.

The results in Table 3 suggest that drop deformation is promoted when we use a domain size with $W = 4R$. In contrast, the drop does not break up and becomes stable with a deformed shape if we set L large enough and $W \geq 6R$ and $H \geq 6R$. Since the value of D for the domain size $L(8R) \times W(6R) \times H(6R)$ differs by only 1.3% with the value for the domain size of $L(8R) \times W(16R) \times H(16R)$, in the results that follow we set the width to $W = 6R$ and the height to $H = 6R$ to minimize the number of computational grid nodes along those directions. To determine the critical Reynolds number Re_c (with $Ca = 0.3$), we consider a domain size of $L(24R) \times W(6R) \times H(6R)$, and we find that the drop reaches a stable state with deformation parameter $D=0.549$ for $Re = 1.0$, while a value of $Re = 1.1$ leads to drop breakup.

3.3.2. Selecting the appropriate grid size

The grid size and adaptive meshing strategy we adopt are chosen to answer the research question as to the conditions that determine whether a bubble in shear flow will break up. In such a case, we must accurately capture the balance of forces between the (non-local) force exerted from the wall-driven flow acting against the interfacial surface tension force. The accuracy of the “Critical

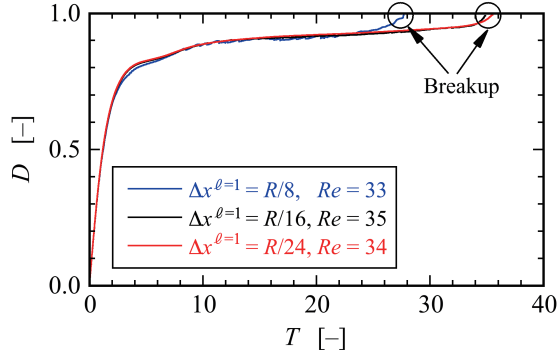


Figure 3: Time evolution of the deformation parameter D versus dimensionless time $T = \Gamma t$ for a bubble, obtained with three grid systems at different resolutions. All three resolutions use a two-level AMR grid with an effective fine resolution grid size $\Delta x^{\ell=1} = \Delta y^{\ell=1} = \Delta z^{\ell=1}$. The evolution of D using the first system, where $\Delta x^{\ell=1} = R/8$, is shown in blue and it predicts that bubble breakup occurs at a Reynolds number $Re = 33$. The evolution of D using the second system, where $\Delta x^{\ell=1} = R/16$, is shown in black and it predicts that bubble breakup occurs at a Reynolds number $Re = 35$. Results with the third system, shown in red, use $\Delta x^{\ell=1} = R/24$, and they predict that breakup occurs at $Re = 34$. The capillary number corresponding to these results is $Ca = 1.0$. ($\lambda = 1.2 \times 10^{-3}$, $\eta < 1.0 \times 10^{-3}$)

441 Reynolds Number” depends on the largest Taylor Deformation parameter D
 442 that is supported by the grid (see e.g., Figures 8 and 11). As we report here,
 443 we have found that as long as the grid size is fine enough to support a Taylor
 444 Deformation parameter $D < 0.95$, then the transition region (i.e. “Critical
 445 Reynolds number”) (see Figures 3 and 12) will be captured with a tolerance
 446 of three percent. The simulation time would become impractical if we were
 447 to try further to improve the accuracy of the “critical Reynolds number”. A
 448 smaller tolerance would necessitate a larger supported Deformation parameter
 449 D , which would in turn, necessitate a higher aspect ratio computational domain,
 450 increased droplet surface area at break-up, increased number of time steps, and
 451 higher resolution for representing the drop/bubble at its thinnest point.

452 We distinguish between our present research and the research found in the
 453 work of Zhang et al. [73, 74] on predicting the conditions for bubble mergers.
 454 Even in the most extreme cases for mergers, the largest Deformation
 455 parameter never exceeds 0.4 in Zhang et al. [73]. In summary, our gridding re-
 456 quirements necessitate grid points distributed relatively evenly throughout the
 457 computational domain when a bubble is stretched to a $D = 0.9$ Deformation,
 458 whereas in Zhang et al. [73], the gridding strategy necessitates a more localized
 459 approach.

460 The numerical results presented in this and the previous section used a
 461 finest-level grid size set to $\Delta x^{\ell=1} (= \Delta y^{\ell=1} = \Delta z^{\ell=1}) = R/16$. To verify the
 462 adequacy of this grid resolution, we present grid refinement results for a bubble
 463 breakup simulation with $Ca = 1.0$, which corresponds to the most deformable
 464 and stretchable bubble case considered in our numerical studies. We use three

465 different grid systems, (i) $\Delta x^{\ell=1} = R/8$, (ii) $\Delta x^{\ell=1} = R/16$, and (iii) $\Delta x^{\ell=1} = R/24$, in order to determine Re_c . Figure 3 shows the time evolution of the
 466 deformation parameter D over time for the three grid systems; the x -axis is a
 467 dimensionless time defined by $T = \Gamma t$ and the y -axis is D . The results show that
 468 bubble breakup occurs at $Re_c = 35$ for the grid system with $\Delta x^{\ell=1} = R/16$,
 469 while the finer computational grid with $\Delta x^{\ell=1} = R/24$ predicts a critical value of
 470 $Re_c = 34$. For the $\Delta x^{\ell=1} = R/8$ results, it is clear that the $R/8$ resolution is too
 471 coarse to capture the proper break-up time, albeit the critical Reynolds' number,
 472 $Re_c = 33$, was still close to the finer grid resolution cases. Note that although
 473 the time evolution of D for the two finer resolution systems ($R/16$ and $R/24$)
 474 is consistent between the two (the predicted critical Reynolds numbers differ
 475 by $\sim 3\%$), the computational time using the grid system with $\Delta x^{\ell=1} = R/24$
 476 was more than 6 times longer than the one based on the coarser system with
 477 $\Delta x^{\ell=1} = R/16$. We remark that in our search for Re_c , we considered a wide
 478 range of values of Ca , and we found it necessary to use a large L ($\sim 24R$) since
 479 for certain shear flows the bubble can stretch significantly without breaking up.
 480 Nevertheless, for the conditions presented in this section, the results indicate
 481 that our numerical approach, even with a finest-level resolution set to $\Delta x^{\ell=1} =$
 482 $R/16$, is capable of accurately reproducing bubble deformation and breakup
 483 without sacrificing any essential dynamical features.

485 4. Results and Discussion

486 4.1. Drop deformation and breakup

487 To illustrate the differences in deformation and breakup between a drop
 488 and a bubble around critical conditions, we first present numerical results for
 489 drop deformation. The time evolution of drop deformation and breakup in
 490 simple linear shear flow for two conditions is shown in Figure 4.1; the first case,
 491 shown in Figure 4.1(a), uses $Ca = 0.3$ and $Re = 1.0$, while the second case,
 492 depicted in Figure 4.1(b), uses $Ca = 0.3$ and $Re = 1.1$. Using a domain size
 493 of $L(24R) \times W(6R) \times H(6R)$, in the case with $Re = 1.0$, the drop gradually
 494 deforms and finally attains a stable deformed state.

495 After $T = 35.0$, the drop remains a stable deformed state with $D = 0.549$.
 496 Over the same domain, for the case with $Re = 1.1$, the “mother” drop elongates
 497 over time, and the volume at the ends of the deforming drop expands; both ends
 498 become bulb-shaped. As time progresses, particularly over the time interval
 499 $48.4 \leq T \leq 55.2$, a thread-bridge forms between the bulbous ends, and the
 500 thread-bridge becomes thinner. Finally, at around the dimensionless time $T \sim$
 501 56.7, the mother drop breaks up, forming two “daughter” drops through the
 502 pinch-off; one satellite drop is also generated between the pinched-off daughter
 503 drops.

504 4.2. Bubble deformation and breakup

505 Next, we present numerical results that illustrate the conditions that lead to
 506 bubble deformation without breakup and conditions where the bubble deforms

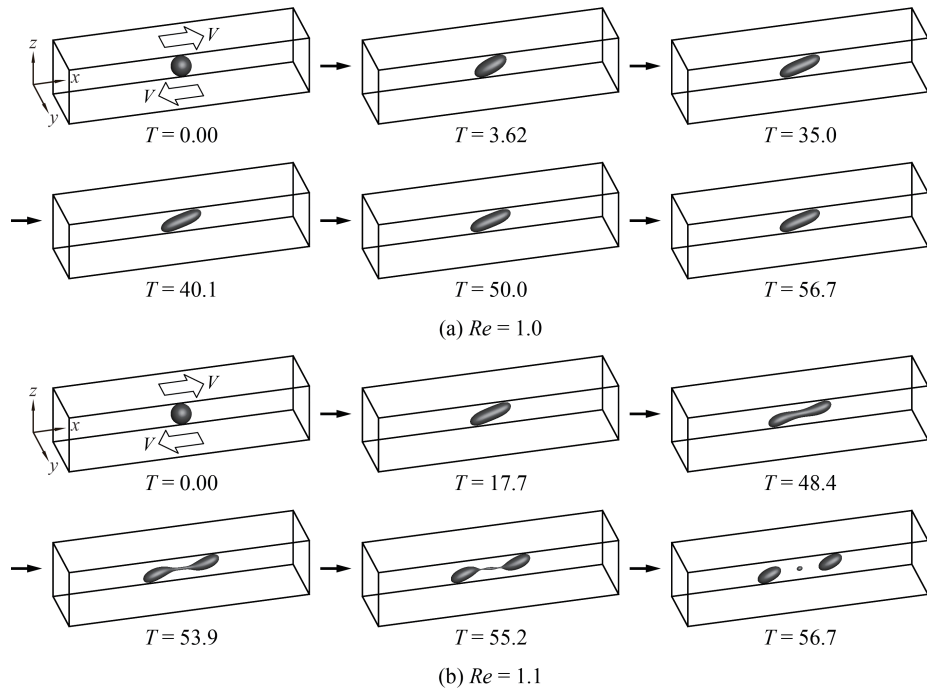


Figure 4: Time evolution of drop deformation and breakup in shear flow at the condition of $Ca = 0.3$ with (a) $Re = 1.0$ and (b) $Re = 1.1$. The “drop” critical Reynolds number corresponding to $Ca = 0.3$ is $1.0 < Re_c < 1.1$. ($\lambda = \eta = 1.0$)

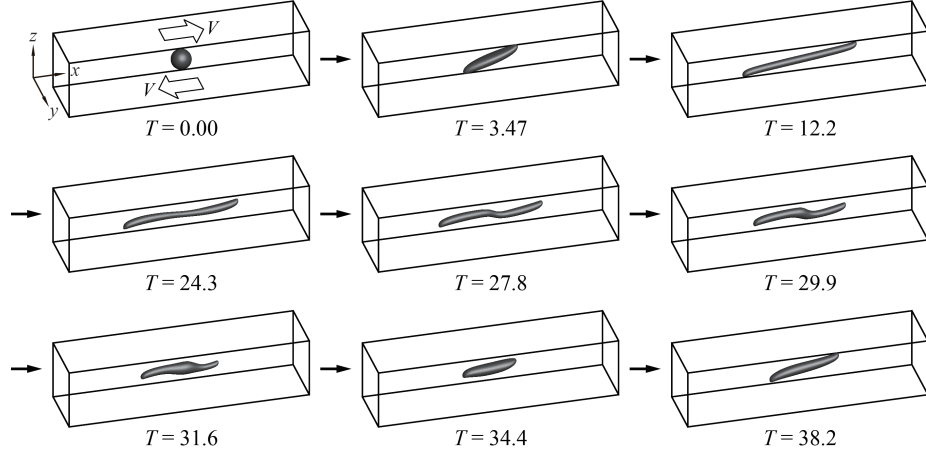


Figure 5: Time evolution of bubble deformation in shear flow at the condition of $Ca = 0.3$ and $Re = 92$. The “bubble” critical Reynolds number corresponding to $Ca = 0.3$ is $92 < Re_c < 93$. In contrast to the drop deformation case, when Re is slightly below Re_c (See Figure 4.1 $Re = 1.0$ for the drop case), the bubble shape will not reach a steady shape, instead the bubble shape alternates between the shapes “slightly stretched” ($T = 3.47$), fully stretched and “doglegged” ($T = 27.8$) and “almost” back to the original “slightly stretched” case ($T = 34.4$). ($\lambda = 1.2 \times 10^{-3}$, $\eta < 1.0 \times 10^{-3}$)

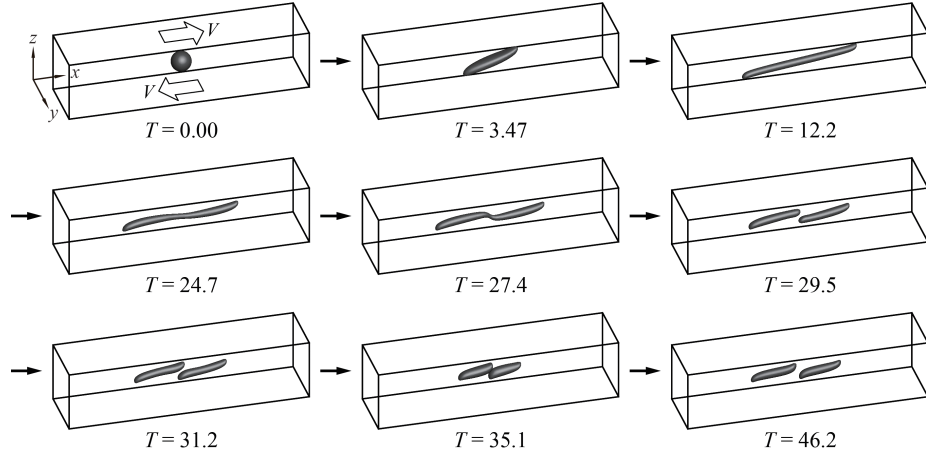


Figure 6: Time evolution of bubble deformation in shear flow at the condition of $Ca = 0.3$ and $Re = 93$. The “bubble” critical Reynolds number corresponding to $Ca = 0.3$ is $92 < Re_c < 93$. ($\lambda = 1.2 \times 10^{-3}$, $\eta < 1.0 \times 10^{-3}$)

507 and ultimately breaks up. The time evolution of shear-induced bubble defor-
508 mation without breakup at the condition of $Ca = 0.3$ and $Re = 92$ is depicted
509 in Figure 5 and the bubble breakup process with flow condition of $Ca = 0.3$
510 and $Re = 93$ is illustrated in Figure 6. The results indicate that the critical
511 Reynolds number is approximately $Re_c = 93$ (with $Ca = 0.3$). A comparison
512 with the drop breakup dynamics presented in Section 4.1 and the correspond-
513 ing processes for bubble deformation and breakup exhibit very distinct features.
514 First, we note that a relatively large shear force magnitude is required for bubble
515 breakup ($\lambda = 1.2 \times 10^{-3}$, $\eta < 1.0 \times 10^{-3}$) compared with the case of the drop (λ
516 $= \eta = 1$). Then, for the same value of $Ca = 0.3$, the critical Reynolds number
517 for the bubble is around 85 times larger than that for the drop. Focusing on the
518 bubble dynamics with no-breakup (Figure 5), the results show that the bub-
519 ble is noticeably elongated in the x -direction at the early stages ($T \leq 24.3$) of
520 bubble deformation, but the bubble does not develop the bulb-like shape (large
521 volume areas) at both ends as observed in the drop deformation process. It is
522 also evident that the ends of the deforming bubble develop cusped shapes under
523 the influence of the strong shear flow.

524 In providing a more detailed description, very large shear forces are required
525 to deform the bubble because $\lambda \simeq 0$ and $\eta \simeq 0$. Thus, the bubble undergoing
526 large shear forces at $T > 0$ is largely stretched along the shear flow direction,
527 and the very long elongated bubble with cusped shapes is formed. Accordingly,
528 the bubble finally breaks up through the elongated shape without forming a
529 bulb-like shape. A noteworthy feature of the non-breaking bubble is that it
530 does not settle into a deformed stable state as in the case of drop deformation
531 presented in Figure 4.1(a). After an initial elongation process, the bubble enters
532 a shrinking phase ($T = 27.8$) where the doglegged shape formed at the center
533 of the bubble returns to a smaller deformed shape ($T = 34.4$) that is similar to
534 its earlier shape ($T = 3.47$). However, when we compare the early deformed
535 bubble shape at $T = 3.47$ with the shape at $T = 34.4$, it is clear that the shapes
536 are not identical. Following the shrinking phase, the bubble stretches again
537 ($T = 38.2$) and oscillates between its elongated shape and shortened geometry.
538

539 For the case of bubble breakup (Figure 6), we observe that the deformation
540 process is almost the same as the no-breakup case until the doglegged shape
541 is formed at $T \sim 27.4$. The bubble finally breaks during the time interval
542 $27.7 \leq T \leq 29.5$. For a closer examination of the bubble breakup process,
543 a detailed panel of cross-sectional slices in the xz -plane through the bubble
544 shape center is presented in Figure 7. The images displayed in Figure 7, which
545 are taken at shorter time intervals than those shown in Fig. 6, reveal that the
546 bubble breaks up into two daughter bubbles due to the pinch off at the thread-
547 bridge part of the doglegged shape during the shrinking process ($T = 28.5 \sim$
548 28.8). After breaking up, the two daughter bubbles migrate to the center: the
549 left daughter bubble moves toward the right side of the domain and the
550 right daughter bubble moves to the left side (see results for $T = 29.5 \sim 35.1$
551 in Figure 6 and for $T = 28.8 \sim 30.9$ in Figure 7). The two daughter bubbles
552 then momentarily congregate near the domain center ($T = 35.1$ in Figure 6),

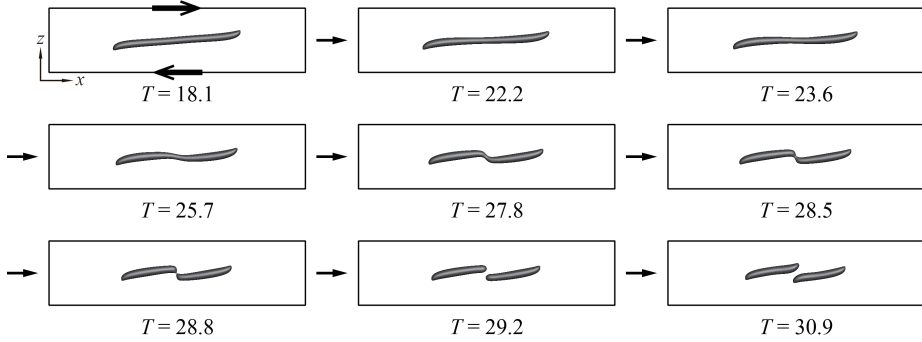


Figure 7: Detail of bubble breakup process in shear flow at the condition of $Ca = 0.3$ and $Re = 93$. The “bubble” critical Reynolds number corresponding to $Ca = 0.3$ is $92 < Re_c < 93$. ($\lambda = 1.2 \times 10^{-3}$, $\eta < 1.0 \times 10^{-3}$)

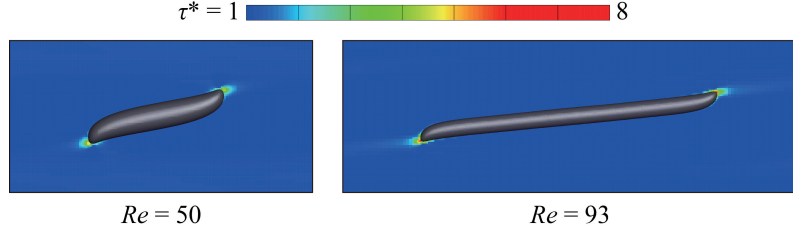


Figure 8: Normalized shear stress τ^* around a bubble for two Reynolds numbers under the condition of $Ca = 0.3$. The left image shows the shear stress profile at $Re = 50$ and the right image at $Re = 93$.

553 before they slowly start to separate: the left daughter bubble moves to the left,
 554 and the right daughter bubble moves to the right ($T = 46.2$ in Figure 6). The
 555 results demonstrate that the bubble breakup process is markedly different from
 556 the analogous drop breakup process with $\lambda = 1$ and $\eta = 1$. Note that the
 557 appearance of deformation and breakup of the drop will largely depend on the
 558 viscosity ratios.

559 *4.3. Shear stress acting on the bubble*

560 The previous section discussed bubble deformation and breakup. Large de-
 561 formation and breakup of the bubble are expected to be closely related to the
 562 state of shear stress acting on the bubble. Figure 8 shows the shear stress profile
 563 for two Reynolds numbers under the condition of $Ca = 0.3$:
 564 Reynolds number equal to 50 and 93. The shear stress profile on the left corre-
 565 sponds to the case of $Re = 50$, and the right side shows the shear stress profile
 566 for the case of $Re = 93$. The normalized shear stress, $\tau^* = \tau/\tau_0$, is defined as
 567 a ratio of the local shear stress $\tau = \mu_m \sqrt{2\mathbf{D} : \mathbf{D}}$ and the apparent shear stress
 568 $\tau_0 = \mu_m \Gamma$. In this study, for a given Ca condition, the same value of τ_0 is used
 569 regardless of Re . For the case of $Re = 50$, the bubble reached a deformed stable

state, and the shear stress profile around the bubble was drawn after the bubble attained a stable deformed state. As observed in previous sections, when the value of Re is slightly below the critical Re condition, the bubble does not settle into a deformed stable state. Instead, it alternates in an elongation and contraction process. The shear stress profile for the case of $Re = 93$ was depicted when the bubble sufficiently elongated ($T = 14.9$). In comparison to the $Re = 50$ case on the left, the right image in Fig. 8 ($Re = 93$) shows a higher shear stress profile near the bubble endpoints as it undergoes an elongation state in the process toward breakup. The value of the maximum shear stress for the case of $Re = 50$ is $\tau^* \approx 6$ and the maximum shear stress for the case of $Re = 93$ at the moment shown in Fig. 8 has the value of $\tau^* \approx 8$. The shear stress profile in Fig. 8 (color contour) is drawn in the range from $\tau^* = 1$ to $\tau^* = 8$, but, for emphasis, shear stress regions with $\tau^* \geq 6$ are illustrated in red. As shown in the figure, the strongest shear stresses are concentrated on the ends of the bubble for both Re conditions. This indicates that the strong shear stresses acting on the ends of the bubble are responsible for much of the bubble stretching. It is important to note that the magnitude of the shear stress acting on the ends of the bubble for the case of $Re = 93$ is much larger than that for the case of $Re = 50$.

We also observed that the shear stress inside the bubble was very small relative to that of the matrix fluid due to the bubble's very small density and viscosity. Since the force of strong shear stresses acting on the ends of the bubble is difficult to transfer across the interface, a sufficiently large Re condition is required for large bubble deformations.

In summary, we discover that for the Reynolds number sufficiently below the critical value, a relatively quick, unsteady elongation period gives way to a steady state (with no break up). On the other hand, for the Reynolds number close to the critical Reynolds number, there is a prolonged, unsteady elongation period in which periodic motion is observed, and the deformation parameter D is close to one. The "vacillating" behavior cannot last forever; ultimately (perhaps stochastically!), the bubble will either settle down or break. Regardless of the outcome, this vacillating behavior will always occur near the critical Reynolds number. In other words, irrespective of the result, we claim, using the grid resolution of $R/16$, that one is assured of being within 3 percent of the critical Reynolds number (see Figure 3). We hypothesize that there will always be "vacillating" behavior if one is sufficiently close to the critical Reynolds number. In other words, given an almost infinite supply of computational resources, as one hones in closer and closer to the critical Reynolds number, a "tug of war" will be observed between the surface tension force trying to pull the bubble together versus the wall driven shear stress trying to pull the bubble apart.

4.4. Velocity field outside and inside the breaking bubble

This section considers the fluid flow velocity field outside and inside the bubble during the shear-induced breakup process. Detailed velocity fields of the deforming and breaking drop have already been presented in a few references (Li et al. [33], Renardy and Cristini [47]). The behavior of the breakup process will influence the velocity fields for the drop and the bubble, so the velocity

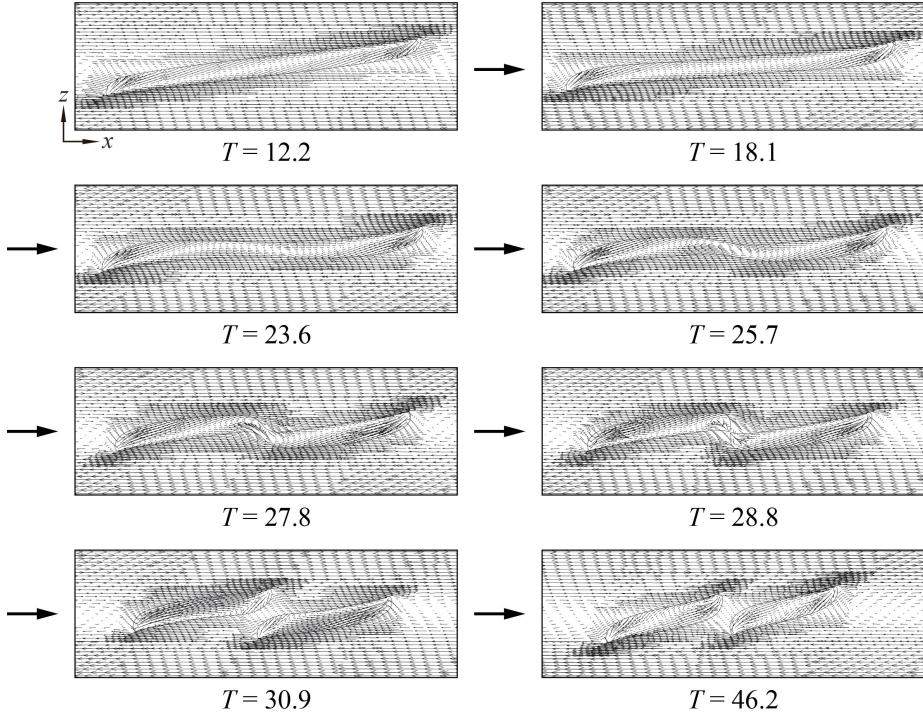


Figure 9: Fluid velocity field outside and inside the breaking bubble in shear flow at the condition $Ca = 0.3$ and $Re = 93$. The “bubble” critical Reynolds number corresponding to $Ca = 0.3$ is $92 < Re_c < 93$. ($\lambda = 1.2 \times 10^{-3}$, $\eta < 1.0 \times 10^{-3}$)

fields for the drop and the bubble are not similar. Figure 9 shows the velocity fields outside and inside the bubble at cross-sectional slices in the xz -plane for a flow condition of $Ca = 0.3$ and $Re = 93$. Regions around the bubble with a higher density of velocity vectors correspond to the level-1 grid portion of the AMR structure. The simulation results show that the velocity field inside the bubble is notably distinct from the surrounding flow field on the bubble’s exterior. The cross-sections at $T = 12.2$ and $T = 18.1$, taken during the elongation phase, show how shear forces at the lower and upper halves of the bubble act along the bottom and top surfaces, respectively, to deform the interface. Near the left and right edges of the bubble, inward interior flows (that point toward the bubble center) begin to develop. Strong shearing forces in the exterior near the bottom-left-end and top-right-end of the bubble interact with the interior flow field through the boundary to create cusped shapes at the bottom-left and top-right ends of the bubble. At the same time, the interface is laterally elongated in the x -direction. During the shrinking process, which occurs for $23.6 \leq T \leq 27.8$, inward flows within the bubble extend over a wider region and are no longer localized near the bubble edges. Then, we observe that circulating flows form at the thread-bridge part of the doglegged

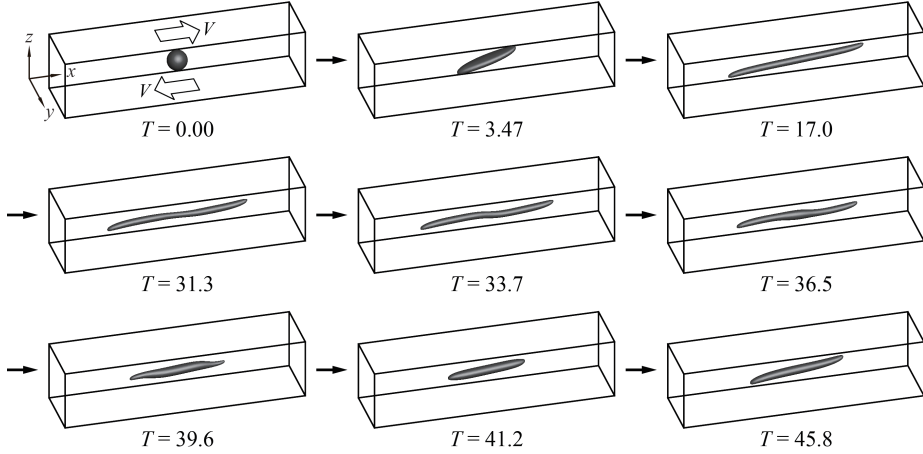


Figure 10: Time evolution of bubble deformation in shear flow at the condition of $Ca = 0.8$ and $Re = 42$. The “bubble” critical Reynolds number corresponding to $Ca = 0.8$ is $42 < Re_c < 43$. ($\lambda = 1.2 \times 10^{-3}$, $\eta < 1.0 \times 10^{-3}$)

633 bubble shape over the time interval [25.7, 27.8]. During the breakup process
 634 ($T \sim 28.8$), higher-intensity inward flows are formed inside the bubble, near the
 635 pinch-off region, that are naturally larger than the surrounding interior flows
 636 and which are inextricably associated with the bubble migration illustrated in
 637 Figs. 6 and 7. As time proceeds further ($T = 46.2$), distinct inward flows
 638 are formed inside the daughter bubbles; the bubbles then migrate toward the
 639 side walls. For example, considering the left daughter bubble, we see that the
 640 mechanism responsible for this movement results from larger shear forces acting
 641 on the bottom-left end than those in the top-left end.

642 4.5. Effect of surface tension on bubble deformation and breakup

643 In previous sections, we considered numerical simulations of bubble deformation
 644 and breakup with a capillary number $Ca = 0.3$. In this section, we examine
 645 the case of $Ca = 0.8$. We investigate the effect of interfacial tension on bubble
 646 deformation and breakup. Using $Ca = 0.8$ for both cases, Figures 10 and 11
 647 present the time evolution of shear-induced bubble deformation and breakup
 648 with $Re = 42$ and $Re = 43$, respectively. We note that the bubble critical
 649 Reynolds number is around $Re_c \approx 43$, whereas $Re_c \approx 0$ for the corresponding
 650 case of the drop with $\lambda = \eta = 1$ (see e.g. Li et al. [33]). Note that Re_c for
 651 $Ca = 0.8$ is smaller than that for the condition of $Ca = 0.3$ since the bubble
 652 at $Ca = 0.8$ is more elastic due to the weaker effect of surface tension in this
 653 case. The results shown in Figs. 10 and 11 indicate that the bubble deforma-
 654 tion and breakup process for the condition of $Ca = 0.8$ is analogous to that for
 655 $Ca = 0.3$. For the case of bubble deformation without breakup (Fig. 10), the
 656 bubble initially assumes a long elongated shape along the x -direction at around
 657 $T = 17.0$. The bubble then enters a compression stage over the time interval

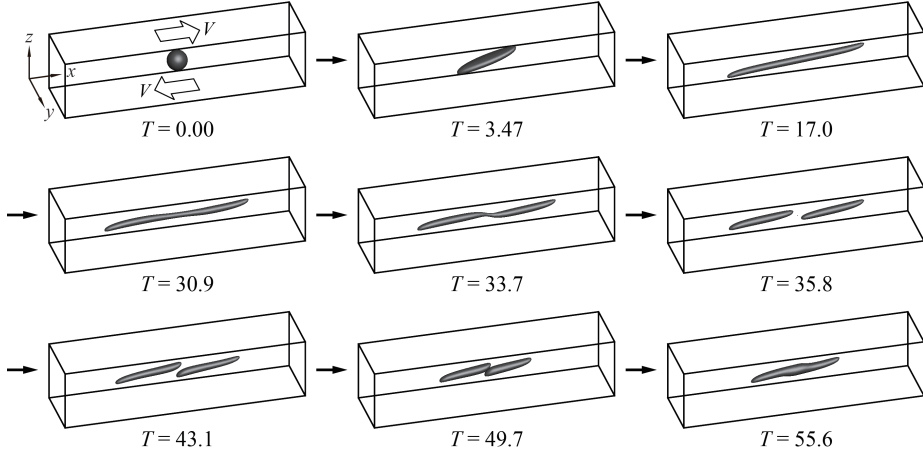


Figure 11: Time evolution of bubble deformation in shear flow at the condition of $Ca = 0.8$ and $Re = 43$. The “bubble” critical Reynolds number corresponding to $Ca = 0.8$ is $42 < Re_c < 43$. ($\lambda = 1.2 \times 10^{-3}$, $\eta < 1.0 \times 10^{-3}$)

[31.3, 41.2] and then elongates again at $T = 45.8$. On the other hand, for the case of bubble breakup (Fig. 11), an initial elongation phase is followed by a doglegged shape formation at $T = 33.7$. After that, the bubble ruptures from the thread-bridge part of the doglegged shape, producing two daughter bubbles ($T = 35.8$). The two daughter bubbles formed after the breakup move to the central area ($T = 49.7$) as in the case of $Ca = 0.8$ and $Re = 93$. Still, the two bubbles eventually coalesce in a region approximately centered in the computational domain ($T = 55.6$). We note that bubbles may coalesce after breaking up in a real experimental setting due to slight deviations in flow conditions and states. Although the process of bubble deformation and breakup for flow conditions with $Ca = 0.3$ and $Ca = 0.8$ are similar, a pronounced difference is that the bubble for $Ca = 0.8$ is more elongated and slender than that for $Ca = 0.3$ due to the smaller effect of surface tension for $Ca = 0.8$.

Table 4 lists, for representative Ca values, the corresponding critical Reynolds number, Re_c , for shear-induced bubble breakup. The data in Table 4 corresponds to $\lambda = 1.2 \times 10^{-3}$, $\eta < 1.0 \times 10^{-3}$, $0.3 < Ca < 1$, and the initial/boundary conditions are given by (1). The results in Table 4 indicate that sufficiently large shear forces are required for bubble breakup, even for large capillary numbers. In Figure 12 we plot the smooth interpolant of the data given in Table 4 and make the hypothesis that given a new data point, (Ca, Re) , shear-induced bubble break up will occur if the point (Ca, Re) is above the given critical curve, and the bubble will not break if the (Ca, Re) pair is below the critical curve. For comparison, a critical curve for the drop with $\lambda = \eta = 1$ is also indicated in Fig. 12. Including breakup and no-breakup critical curves for both the drop and the bubble will facilitate future identification of Re_c numbers and, thus, a complete general critical curve for a wide range of Ca numbers.

Table 4: Shear-induced bubble breakup for various flow conditions described in terms of column pairs of critical Reynolds numbers and corresponding capillary numbers. ($\lambda = 1.2 \times 10^{-3}$, $\eta < 1.0 \times 10^{-3}$)

Capillary number Ca	0.3	0.5	0.8	1.0
Critical Reynolds number Re_c	93	67	43	35

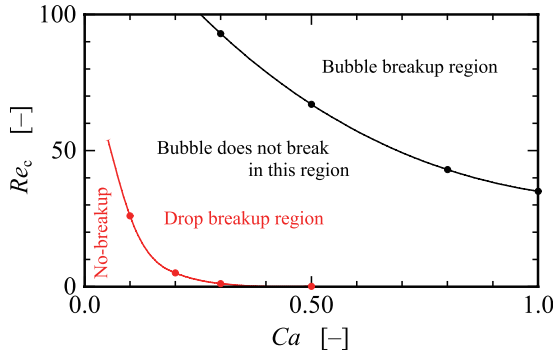


Figure 12: A plot of the critical Reynolds number versus capillary number for the data listed in Table 4. $\lambda = 1.2 \times 10^{-3}$, $\eta < 1.0 \times 10^{-3}$, $0.3 < Ca < 1$, and the initial/boundary conditions are given by (1). Given a new data point, (Ca, Re) , one can reliably predict whether the given (Ca, Re) pair will result in shear induced bubble break-up or not. Note, for the “Drop delineation curve,” $\lambda = \eta = 1$.

684 5. Conclusions

685 The bubble deformation and breakup process in liquid due to a driving
 686 simple linear shear flow was explored numerically using the CLSVOF computational
 687 method. In this study, the critical Reynolds number Re_c , at which
 688 bubble breakup first occurs, was determined for several flow conditions, and the
 689 differences between the morphology of bubble deformation and breakup were
 690 compared with the analogous morphology of drop deformation and breakup.

691 The numerical results revealed significant differences between bubble de-
 692 formation and breakup and the corresponding drop dynamics. For the case
 693 of a bubble, it was discovered that much stronger shear flows are necessary
 694 to induce interface breakup compared with a drop immersed in a similar flow
 695 field. That is, a much larger Reynolds number flow is required to induce bubble
 696 breakup. The steps leading to bubble breakup were similar throughout the Ca
 697 number range considered in our computations: the bubble underwent a simi-
 698 lar breakup mechanism in which rupture occurred at a thread-bridge part that
 699 followed a doglegged shape formation stage. For bubble deformation without
 700 breakup, near Re_c , the bubble did not maintain a stable deformed shape, unlike
 701 drop deformation near the critical Reynolds number. The bubble exhibited pro-
 702 nounced underdamped behavior: the bubble oscillated between elongating and
 703 shrinking motions for non-rupturing flow conditions. At the same time, bubble
 704 deformation under smaller Re conditions ($< Re_c$) led to a stable state. Com-

pared with the drop, we attribute the significant differences in morphology for the bubble undergoing breakup to the density and viscosity ratio. Due to the bubble's very small density and viscosity, it is comparatively difficult to transfer the shear stresses acting on the ends of the bubble across the interface.

There are several directions for future work. In the present work, we varied the capillary number and Reynolds number to study bubble deformation and breakup morphology in the presence of a simple shear flow. For the future, one can also vary (i) the viscosity ratio, (ii) the effect of the initial shape of the bubble[39], (iii) the magnitude and direction of the gravitational force, (iv) the non-Newtonian properties of the “matrix” liquid, (v) bubble deformation and breakup due to a shear flow in a T junction[16], (vi) bubble deformation and breakup confined shear flow (see [18] for the drop case), and (vii) bubble deformation and breakup due to non-uniform shear flow (see [6] for the drop case).

References

- [1] Amani, A., Balcázar, N., Castro, J., Oliva, A., 2019. Numerical study of droplet deformation in shear flow using a conservative level-set method. *Chemical Engineering Science* 207, 153–171. URL: <http://www.sciencedirect.com/science/article/pii/S0009250919305123>, doi:<https://doi.org/10.1016/j.ces.2019.06.014>.
- [2] Arienti, M., Li, X., Soteriou, M., Eckett, C., Sussman, M., Jensen, R., 2013. Coupled level-set/volume-of-fluid method for simulation of injector atomization. *Journal of propulsion and power* 29, 147–157.
- [3] Bazhlekov, I.B., Anderson, P.D., Meijer, H.E., 2006. Numerical investigation of the effect of insoluble surfactants on drop deformation and breakup in simple shear flow. *Journal of Colloid and Interface Science* 298, 369 – 394. URL: <http://www.sciencedirect.com/science/article/pii/S0021979705012658>, doi:<http://dx.doi.org/10.1016/j.jcis.2005.12.017>.
- [4] Bento, D., Rodrigues, R.O., Faustino, V., Pinho, D., Fernandes, C.S., Pereira, A.I., Garcia, V., Miranda, J.M., Lima, R., 2018. Deformation of red blood cells, air bubbles, and droplets in microfluidic devices: Flow visualizations and measurements. *Micromachines* 9, 151. URL: <https://www.mdpi.com/2072-666X/9/4/151>, doi:10.3390/mi9040151.
- [5] Canedo, E.L., Favelukis, M., Tadmor, Z., Talmon, Y., 1993. An experimental study of bubble deformation in viscous liquids in simple shear flow. *AIChE Journal* 39, 553–559. URL: <https://aiche.onlinelibrary.wiley.com/doi/abs/10.1002/aic.690390403>, doi:<https://doi.org/10.1002/aic.690390403>, arXiv:<https://aiche.onlinelibrary.wiley.com/doi/pdf/10.1002/aic.690390403>.

- 746 [6] Chin, H.B., Han, C.D., 1980. Studies on droplet deformation and breakup.
 747 ii. breakup of a droplet in nonuniform shear flow. *Journal of rheology* 24,
 748 1–37.
- 749 [7] Chu, P., Finch, J., Bournival, G., Ata, S., Hamlett, C., Pugh, R.J.,
 750 2019. A review of bubble break-up. *Advances in Colloid and Interface
 751 Science* 270, 108–122. URL: <https://www.sciencedirect.com/science/article/pii/S0001868619300211>, doi:<https://doi.org/10.1016/j.cis.2019.05.010>.
- 754 [8] Cristini, V., Bławzdziewicz, J., Loewenberg, M., 2001. An adaptive
 755 mesh algorithm for evolving surfaces: simulations of drop breakup
 756 and coalescence. *Journal of Computational Physics* 168, 445 –
 757 463. URL: <http://www.sciencedirect.com/science/article/pii/S0021999101967130>, doi:<http://dx.doi.org/10.1006/jcph.2001.6713>.
- 759 [9] Cristini, V., Guido, S., Alfani, A., Bławzdziewicz, J., Loewenberg, M.,
 760 2003. Drop breakup and fragment size distribution in shear flow. *Journal
 761 of Rheology* 47, 1283–1298. URL: <http://scitation.aip.org/content/sor/journal/jor2/47/5/10.1122/1.1603240>, doi:<http://dx.doi.org/10.1122/1.1603240>.
- 764 [10] Croce, R., Griebel, M., Schweitzer, M.A., 2010. Numerical simulation of
 765 bubble and droplet deformation by a level set approach with surface tension
 766 in three dimensions. *International Journal for Numerical Methods in Fluids*
 767 62, 963–993. URL: <http://dx.doi.org/10.1002/fld.2051>, doi:10.1002/fld.2051.
- 769 [11] Drenckhan, W., Saint-Jalmes, A., 2015. The science of foaming. *Advances
 770 in Colloid and Interface Science* 222, 228–259. URL: <https://www.sciencedirect.com/science/article/pii/S0001868615000603>,
 771 doi:<https://doi.org/10.1016/j.cis.2015.04.001>. reinhard Miller,
 773 Honorary Issue.
- 774 [12] Eftekhari, M., Schwarzenberger, K., Heitkam, S., Eckert, K.,
 775 2021a. Interfacial flow of a surfactant-laden interface under asym-
 776 metric shear flow. *Journal of Colloid and Interface Science* 599,
 777 837–848. URL: <https://www.sciencedirect.com/science/article/pii/S0021979721006457>, doi:<https://doi.org/10.1016/j.jcis.2021.04.126>.
- 780 [13] Eftekhari, M., Schwarzenberger, K., Heitkam, S., Javadi, A.,
 781 Bashkatov, A., Ata, S., Eckert, K., 2021b. Interfacial be-
 782 havior of particle-laden bubbles under asymmetric shear flow.
 783 *Langmuir* 37, 13244–13254. URL: <https://doi.org/10.1021/acs.langmuir.1c01814>,
 784 doi:10.1021/acs.langmuir.1c01814, arXiv:<https://doi.org/10.1021/acs.langmuir.1c01814>. pMID:
 786 34726918.

- 787 [14] Ervin, E., Tryggvason, G., 1997. The rise of bubbles in a vertical shear
 788 flow. *Journal of Fluids Engineering* 119(2), 443–449.
- 789 [15] Fang, Z., Shuai, Y., Huang, Z., Wang, J., Yang, Y., 2024. Inten-
 790 sification of polyethylene devolatilization in twin-screw extruder
 791 with additives. *Polymer Engineering & Science* 64, 2961–2974.
 792 URL: <https://4spepublications.onlinelibrary.wiley.com/doi/abs/10.1002/pen.26738>,
 793 doi:<https://doi.org/10.1002/pen.26738>,
 794 arXiv:<https://4spepublications.onlinelibrary.wiley.com/doi/pdf/10.1002/pen.26738>.
- 795 [16] Frense, E., Rüdiger, F., Fröhlich, J., 2024. Modeling of dynamic bub-
 796 ble deformation and breakup in t-junction channel flow. *Chemical En-
 797 gineering Science* 300, 120579. URL: <https://www.sciencedirect.com/science/article/pii/S0009250924008790>, doi:<https://doi.org/10.1016/j.ces.2024.120579>.
- 800 [17] Gao, S., Shi, Y., Pan, G., Quan, X., 2022. Research on the
 801 effect of asymmetric bubbles on the load characteristics of projec-
 802 tiles during an underwater salvo. *Applied Ocean Research* 124,
 803 103212. URL: <https://www.sciencedirect.com/science/article/pii/S0141118722001535>, doi:<https://doi.org/10.1016/j.apor.2022.103212>.
- 806 [18] Gupta, A., Sbragaglia, M., 2014. Deformation and breakup of viscoelastic
 807 droplets in confined shear flow. *Physical Review E* 90, 023305.
- 808 [19] Hernandez, F.H., Rangel, R.H., 2017. Breakup of drops in simple
 809 shear flows with high-confinement geometry. *Computers & Fluids* 146,
 810 23 – 41. URL: <http://www.sciencedirect.com/science/article/pii/S0045793017300038>, doi:<https://doi.org/10.1016/j.compfluid.2017.01.001>.
- 813 [20] Hirt, C., Nichols, B., 1981. Volume of fluid (vof) method
 814 for the dynamics of free boundaries. *Journal of Computational
 815 Physics* 39, 201 – 225. URL: <http://www.sciencedirect.com/science/article/pii/0021999181901455>, doi:[http://dx.doi.org/10.1016/0021-9991\(81\)90145-5](http://dx.doi.org/10.1016/0021-9991(81)90145-5).
- 818 [21] Hoyt, N.C., 2013. The performance of passive cyclonic separators in mi-
 819 crogravity. Case Western Reserve University.
- 820 [22] Inamuro, T., 2006. Lattice boltzmann methods for viscous fluid flows and
 821 for two-phase fluid flows. *Fluid Dynamics Research* 38, 641. URL: <http://stacks.iop.org/1873-7005/38/i=9/a=A04>.
- 823 [23] Inamuro, T., Tomita, R., Ogino, F., 2003. Lattice boltzmann sim-
 824 lations of drop deformation and breakup in simple shear flows. *Inter-
 825 national Journal of Modern Physics B* 17, 21–26. URL: <http://www.worldscientific.com/doi/abs/10.1142/S0217979203017035>, doi:[10.1142/S0217979203017035](http://dx.doi.org/10.1142/S0217979203017035).

- 828 [24] Ioannou, N., Liu, H., Zhang, Y., 2016. Droplet dynamics
 829 in confinement. Journal of Computational Science 17, 463 –
 830 474. URL: <http://www.sciencedirect.com/science/article/pii/S1877750316300308>, doi:<https://doi.org/10.1016/j.jocs.2016.03.009>. discrete Simulation of Fluid Dynamics 2015.
- 833 [25] Janssen, P., Anderson, P., 2008. A boundary-integral model for
 834 drop deformation between two parallel plates with non-unit viscosity
 835 ratio drops. Journal of Computational Physics 227, 8807–
 836 8819. URL: <http://www.sciencedirect.com/science/article/pii/S002199910800346X>, doi:<http://dx.doi.org/10.1016/j.jcp.2008.06.027>.
- 839 [26] Janssen, P.J.A., Anderson, P.D., 2007. Boundary-integral method
 840 for drop deformation between parallel plates. Physics of Fluids
 841 19. URL: <http://scitation.aip.org/content/aip/journal/pof2/19/4/10.1063/1.2715621>, doi:<http://dx.doi.org/10.1063/1.2715621>.
- 843 [27] Kang, M., Fedkiw, R.P., Liu, X.D., 2000. A boundary condition capturing
 844 method for multiphase incompressible flow. Journal of scientific computing
 845 15, 323–360.
- 846 [28] Khismatullin, D.B., Renardy, Y., Cristini, V., 2003. Inertia-induced
 847 breakup of highly viscous drops subjected to simple shear. Physics of Fluids
 848 15, 1351–1354. doi:<http://dx.doi.org/10.1063/1.1564825>.
- 849 [29] Komrakova, A., Shardt, O., Eskin, D., Derksen, J., 2014. Lattice
 850 boltzmann simulations of drop deformation and breakup in shear flow.
 851 International Journal of Multiphase Flow 59, 24 – 43. URL: <http://www.sciencedirect.com/science/article/pii/S0301932213001547>,
 852 doi:<http://dx.doi.org/10.1016/j.ijmultiphaseflow.2013.10.009>.
- 854 [30] Komrakova, A., Shardt, O., Eskin, D., Derksen, J., 2015. Effects
 855 of dispersed phase viscosity on drop deformation and breakup
 856 in inertial shear flow. Chemical Engineering Science 126, 150 –
 857 159. URL: <http://www.sciencedirect.com/science/article/pii/S000925091400726X>, doi:<http://dx.doi.org/10.1016/j.ces.2014.12.012>.
- 860 [31] Legendre, D., Magnaudet, J., 1998. The lift force on a spherical bubble in
 861 a viscous linear shear flow. Journal of Fluid Mechanics 368, 81–126.
- 862 [32] Lewin-Jones, P., Lockerby, D.A., Sprittles, J.E., 2024. Collision of liquid
 863 drops: bounce or merge? Journal of Fluid Mechanics 995, A1. doi:[10.1017/jfm.2024.722](https://doi.org/10.1017/jfm.2024.722).
- 865 [33] Li, J., Renardy, Y., Renardy, M., 2000. Numerical simulation of
 866 breakup of a viscous drop in simple shear flow through a volume-of-fluid
 867 method. Physics of Fluids 12, 269–282. URL: <http://scitation.aip>.

- 868 [org/content/aip/journal/pof2/12/2/10.1063/1.870305](http://dx.doi.org/10.1063/1.870305), doi:<http://dx.doi.org/10.1063/1.870305>.
- 870 [34] Li, X., Soteriou, M.C., 2016. High fidelity simulation and analysis of liq-
871 uid jet atomization in a gaseous crossflow at intermediate weber numbers.
872 Physics of Fluids 28.
- 873 [35] Lohse, D., 2018. Bubble puzzles: from fundamentals to applications. Physical
874 review fluids 3, 110504.
- 875 [36] Müller-Fischer, N., Tobler, P., Dressler, M., Fischer, P., Windhab, E.J.,
876 2008. Single bubble deformation and breakup in simple shear flow. Experi-
877 ments in fluids 45, 917–926.
- 878 [37] Ohta, M., Akama, Y., Yoshida, Y., Sussman, M., 2014. Influence of the
879 viscosity ratio on drop dynamics and breakup for a drop rising in an im-
880 miscible low-viscosity liquid. Journal of Fluid Mechanics 752, 383–409.
881 doi:[10.1017/jfm.2014.339](https://doi.org/10.1017/jfm.2014.339).
- 882 [38] Ohta, M., Furukawa, T., Yoshida, Y., Sussman, M., 2019. A
883 three-dimensional numerical study on the dynamics and deformation
884 of a bubble rising in a hybrid carreau and fene-cr modeled poly-
885 mERIC liquid. Journal of Non-Newtonian Fluid Mechanics 265, 66–
886 78. URL: <https://www.sciencedirect.com/science/article/pii/S0377025718301952>, doi:<https://doi.org/10.1016/j.jnnfm.2018.12.012>.
- 889 [39] Ohta, M., Imura, T., Yoshida, Y., Sussman, M., 2005. A computational
890 study of the effect of initial bubble conditions on the motion of a gas bubble
891 rising in viscous liquids. International journal of multiphase flow 31, 223–
892 237.
- 893 [40] Ohta, M., Kikuchi, D., Yoshida, Y., Sussman, M., 2011. Robust numeri-
894 cal analysis of the dynamic bubble formation process in a viscous liquid.
895 International Journal of Multiphase Flow 37, 1059–1071.
- 896 [41] Ohta, M., Sussman, M., 2012. The buoyancy-driven mo-
897 tion of a single skirted bubble or drop rising through
898 a viscous liquid. Physics of Fluids 24, 112101. URL:
899 <https://doi.org/10.1063/1.4765669>, doi:[10.1063/1.4765669](https://doi.org/10.1063/1.4765669),
900 arXiv:https://pubs.aip.org/aip/pof/article-pdf/doi/10.1063/1.4765669/14128560/112101_1.pdf
- 901 [42] Ohta, M., Yamaguchi, S., Yoshida, Y., Sussman, M., 2010. The sensitivity
902 of drop motion due to the density and viscosity ratio. Physics of Fluids 22.
- 903 [43] Rallison, J.M., 1984. The deformation of small viscous drops
904 and bubbles in shear flows. Annual Review of Fluid Mechan-
905 ics 16, 45–66. URL: <http://dx.doi.org/10.1146/annurev.fl.16.010184.000401>,
906 doi:[10.1146/annurev.fl.16.010184.000401](https://doi.org/10.1146/annurev.fl.16.010184.000401),
907 arXiv:<http://dx.doi.org/10.1146/annurev.fl.16.010184.000401>.

- 908 [44] Renardy, Y., 2006. Numerical simulation of a drop undergoing large am-
909 plitude oscillatory shear. *Rheologica acta* 45, 223–227.
- 910 [45] Renardy, Y., 2007. The effects of confinement and inertia on the production
911 of droplets. *Rheologica Acta* 46, 521–529. URL: <http://dx.doi.org/10.1007/s00397-006-0150-y>, doi:<http://dx.doi.org/10.1007/s00397-006-0150-y>.
- 913 [46] Renardy, Y., 2008. Effect of startup conditions on drop breakup
914 under shear with inertia. *International Journal of Multiphase Flow* 34, 1185 – 1189. URL: <http://www.sciencedirect.com/science/article/pii/S030193220800089X>, doi:<http://dx.doi.org/10.1016/j.ijmultiphaseflow.2008.04.004>.
- 918 [47] Renardy, Y., Cristini, V., 2001a. Effect of inertia on drop breakup under
919 shear. *Physics of Fluids* 13, 7–13. URL: <http://scitation.aip.org/content/aip/journal/pof2/13/1/10.1063/1.1331321>, doi:<http://dx.doi.org/10.1063/1.1331321>.
- 922 [48] Renardy, Y., Cristini, V., Li, J., 2002. Drop fragment distributions un-
923 der shear with inertia. *International Journal of Multiphase Flow* 28, 1125
924 – 1147. URL: <http://www.sciencedirect.com/science/article/pii/S0301932202000228>, doi:[http://dx.doi.org/10.1016/S0301-9322\(02\)00022-8](http://dx.doi.org/10.1016/S0301-9322(02)00022-8).
- 927 [49] Renardy, Y.Y., Cristini, V., 2001b. Scalings for fragments produced
928 from drop breakup in shear flow with inertia. *Physics of Fluids* 13,
929 2161–2164. URL: <https://doi.org/10.1063/1.1384469>, doi:[10.1063/1.1384469](https://doi.org/10.1063/1.1384469), arXiv:<https://doi.org/10.1063/1.1384469>.
- 931 [50] Rust, A., Manga, M., 2002. Bubble shapes and orientations in low re-
932 simple shear flow. *Journal of Colloid and Interface Science* 249, 476–
933 480. URL: <https://www.sciencedirect.com/science/article/pii/S0021979702982925>, doi:<https://doi.org/10.1006/jcis.2002.8292>.
- 935 [51] Sanogo, B., Souidi, K., Marcati, A., Vial, C., 2023. Food aeration: Ef-
936 fect of the surface-active agent type on bubble deformation and break-up
937 in a viscous newtonian fluid: From single bubble to process-scale. *Food*
938 *Research International* 165, 112478. URL: <https://www.sciencedirect.com/science/article/pii/S0963996923000236>, doi:<https://doi.org/10.1016/j.foodres.2023.112478>.
- 941 [52] Schlüter, M., Herres-Pawlis, S., Nieken, U., Tuttlies, U., Bothe, D., 2021.
942 Small-scale phenomena in reactive bubbly flows: Experiments, numerical
943 modeling, and applications. *Annual review of chemical and biomolecular
944 engineering* 12, 625–643.
- 945 [53] Sharifi, R., Varmazyan, M., Mohammadi, A., 2024. Investigat-
946 ing droplet and bubble deformation under shear flow us-
947 ing the multi-pseudo-potential scheme of lattice boltzmann

- 948 method. Advances in Applied Mathematics and Mechanics
 949 16, 519–548. URL: <https://global-sci.com/article/72820/investigating-droplet-and-bubble-deformation-under-shear-flow-using-the-multi-pseudo-p>
 950 doi:<https://doi.org/10.4208/aamm.OA-2021-0326>.
- 952 [54] Sines, J.N., Straiton, B.J., Zuccarelli, C.E., Marashdeh, Q.M., Teixeira,
 953 F.L., Fan, L.S., Motil, B.J., 2020. Study of gas-water flow inside
 954 of a horizontal passive cyclonic gas-liquid phase separator system using
 955 displacement-current phase tomography. Gravitational and Space Research
 956 6, 28–43.
- 957 [55] Stewart, P., Lay, N., Sussman, M., Ohta, M., 2008. An improved sharp
 958 interface method for viscoelastic and viscous two-phase flows. Journal of
 959 Scientific Computing 35, 43–61.
- 960 [56] Stone, H.A., 1994. Dynamics of drop deformation and breakup
 961 in viscous fluids. Annual Review of Fluid Mechanics 26,
 962 65–102. URL: <http://dx.doi.org/10.1146/annurev.fl.26.010194.000433>,
 963 doi:[10.1146/annurev.fl.26.010194.000433](https://doi.org/10.1146/annurev.fl.26.010194.000433),
 964 arXiv:<http://dx.doi.org/10.1146/annurev.fl.26.010194.000433>.
- 965 [57] Sussman, M., 2003. A second order coupled level set and volume-
 966 of-fluid method for computing growth and collapse of vapor bubbles.
 967 Journal of Computational Physics 187, 110–136. URL: <https://www.sciencedirect.com/science/article/pii/S0021999103000871>,
 968 doi:[https://doi.org/10.1016/S0021-9991\(03\)00087-1](https://doi.org/10.1016/S0021-9991(03)00087-1).
- 970 [58] Sussman, M., Almgren, A.S., Bell, J.B., Colella, P., Howell, L.H.,
 971 Welcome, M.L., 1999. An adaptive level set approach for incom-
 972 pressible two-phase flows. Journal of Computational Physics 148, 81
 973 – 124. URL: <http://www.sciencedirect.com/science/article/pii/S002199919896106X>, doi:<https://doi.org/10.1006/jcph.1998.6106>.
- 975 [59] Sussman, M., Puckett, E.G., 2000. A coupled level set and
 976 volume-of-fluid method for computing 3d and axisymmetric incompress-
 977 ible two-phase flows. Journal of Computational Physics 162, 301–
 978 337. URL: <http://www.sciencedirect.com/science/article/pii/S0021999100965379>, doi:<https://doi.org/10.1006/jcph.2000.6537>.
- 980 [60] Sussman, M., Smereka, P., Osher, S., 1994. A level set ap-
 981 proach for computing solutions to incompressible two-phase flow.
 982 Journal of Computational Physics 114, 146 – 159. URL: <http://www.sciencedirect.com/science/article/pii/S0021999184711557>,
 983 doi:<https://doi.org/10.1006/jcph.1994.1155>.
- 985 [61] Sussman, M., Smith, K., Hussaini, M., Ohta, M., Zhi-Wei, R., 2007. A
 986 sharp interface method for incompressible two-phase flows. Journal of Com-
 987 putational Physics 221, 469–505. URL: <https://www.sciencedirect.com/science/article/pii/S0021999106008342>.

- 988 com/science/article/pii/S0021999106002981, doi:<https://doi.org/10.1016/j.jcp.2006.06.020>.
- 990 [62] Tanguy, S., Ménard, T., Berlemont, A., 2007. A level set method for
 991 vaporizing two-phase flows. Journal of Computational Physics 221, 837–
 992 853.
- 993 [63] Tatebe, O., 1993. The multigrid preconditioned conjugate gradient method,
 994 in: NASA. Langley Research Center, The Sixth Copper Mountain Confer-
 995 ence on Multigrid Methods, Part 2.
- 996 [64] Taylor, G.I., 1932. The viscosity of a fluid containing small drops of another
 997 fluid. Proceedings of the Royal Society of London A: Mathematical, Phys-
 998 ical and Engineering Sciences 138, 41–48. doi:[10.1098/rspa.1932.0169](https://doi.org/10.1098/rspa.1932.0169).
- 999 [65] Taylor, G.I., 1934. The formation of emulsions in definable fields of flow.
 1000 Proceedings of the Royal Society of London A: Mathematical, Physical and
 1001 Engineering Sciences 146, 501–523. doi:[10.1098/rspa.1934.0169](https://doi.org/10.1098/rspa.1934.0169).
- 1002 [66] Unverdi, S.O., Tryggvason, G., 1992. A front-tracking method
 1003 for viscous, incompressible, multi-fluid flows. Journal of Computa-
 1004 tional Physics 100, 25 – 37. URL: <http://www.sciencedirect.com/science/article/pii/002199919290307K>, doi:[http://dx.doi.org/10.1016/0021-9991\(92\)90307-K](http://dx.doi.org/10.1016/0021-9991(92)90307-K).
- 1007 [67] Wang, A., Evans, G., Mitra, S., 2023. A review of bubble
 1008 surface loading and its effect on bubble dynamics. Minerals
 1009 Engineering 199, 108105. URL: <https://www.sciencedirect.com/science/article/pii/S089268752300119X>, doi:<https://doi.org/10.1016/j.mineng.2023.108105>.
- 1012 [68] Wang, Z., Shi, D., Zhang, A., 2015. Three-dimensional lattice boltz-
 1013 mann simulation of bubble behavior in a flap-induced shear flow. Com-
 1014 puters & Fluids 123, 44 – 53. URL: <http://www.sciencedirect.com/science/article/pii/S0045793015003199>, doi:<https://doi.org/10.1016/j.compfluid.2015.09.007>.
- 1017 [69] Wei, Y.K., Qian, Y., Xu, H., 2012. Lattice boltzmann simulations
 1018 of single bubble deformation and breakup in a shear flow. The Jour-
 1019 nal of Computational Multiphase Flows 4, 111–117. URL: <https://doi.org/10.1260/1757-482X.4.1.111>, doi:[10.1260/1757-482X.4.1.111](https://doi.org/10.1260/1757-482X.4.1.111), arXiv:<https://doi.org/10.1260/1757-482X.4.1.111>.
- 1022 [70] Wong, A., Park, C., 2012. A visualization system for observing
 1023 plastic foaming processes under shear stress. Polymer Testing
 1024 31, 417–424. URL: <https://www.sciencedirect.com/science/article/pii/S0142941811002169>, doi:<https://doi.org/10.1016/j.polymertesting.2011.12.012>.

- 1027 [71] Yoshikawa, H.N., Zoueshtiagh, F., Caps, H., Kurowski, P., Petitjeans, P.,
1028 2010. Bubble splitting in oscillatory flows on ground and in reduced gravity.
1029 The European Physical Journal E 31, 191–199.
- 1030 [72] Zhang, J., Miksis, M.J., Bankoff, S.G., 2006. Nonlinear dynamics of
1031 a two-dimensional viscous drop under shear flow. Physics of Fluids
1032 18. URL: <http://scitation.aip.org/content/aip/journal/pof2/18/7/10.1063/1.2222336>, doi:<http://dx.doi.org/10.1063/1.2222336>.
- 1033 [73] Zhang, J., Ni, M.J., Magnaudet, J., 2021a. Three-dimensional dynamics
1034 of a pair of deformable bubbles rising initially in line. part 1. moderately
1035 inertial regimes. Journal of Fluid Mechanics 920, A16.
- 1036 [74] Zhang, J., Ni, M.J., Magnaudet, J., 2022. Three-dimensional dynamics of
1037 a pair of deformable bubbles rising initially in line. part 2. highly inertial
1038 regimes. Journal of Fluid Mechanics 943, A10.
- 1039 [75] Zhang, J., Shu, S., Guan, X., Yang, N., 2021b. Regime mapping
1040 of multiple breakup of droplets in shear flow by phase-field
1041 lattice boltzmann simulation. Chemical Engineering Science 240,
1042 116673. URL: <https://www.sciencedirect.com/science/article/pii/S0009250921002384>, doi:<https://doi.org/10.1016/j.ces.2021.116673>.
- 1043 [76] Zhang, W., Almgren, A., Beckner, V., Bell, J., Blaschke, J., Chan, C.,
1044 Day, M., Friesen, B., Gott, K., Graves, D., Katz, M., Myers, A., Nguyen,
1045 T., Nonaka, A., Rosso, M., Williams, S., Zingale, M., 2019. AMReX: a
1046 framework for block-structured adaptive mesh refinement. Journal of Open
1047 Source Software 4, 1370. URL: <https://doi.org/10.21105/joss.01370>,
1048 doi:10.21105/joss.01370.
- 1049
- 1050
- 1051